Peering into Batteries: Electrochemical Insight through Operando Methods

Esther S. Takeuchi
SUNY Distinguished Professor
William and Jane Knapp Chair in Energy and the Environment, NAE, NMTI, NAI , NIHF

Departments of Chemistry; Materials Science and Chemical Engineering
Brookhaven National Laboratory; Energy and Photon Sciences

BROOKHAVEN NATIONAL LABORATORY

Stony Brook University

Terminology Relevant to Mechanistic Investigations

Ex-situ

Destructive analysis of a working battery. Parts removed for analysis outside the functional environment.

In-situ

Measurement of property or material in working environment, system may be not operationing at time of measurement.

Operando

Probe of electrochemistry while operational. Ion transport and electron transfer are taking place simultaneously with measurement. Gain information on kinetics.

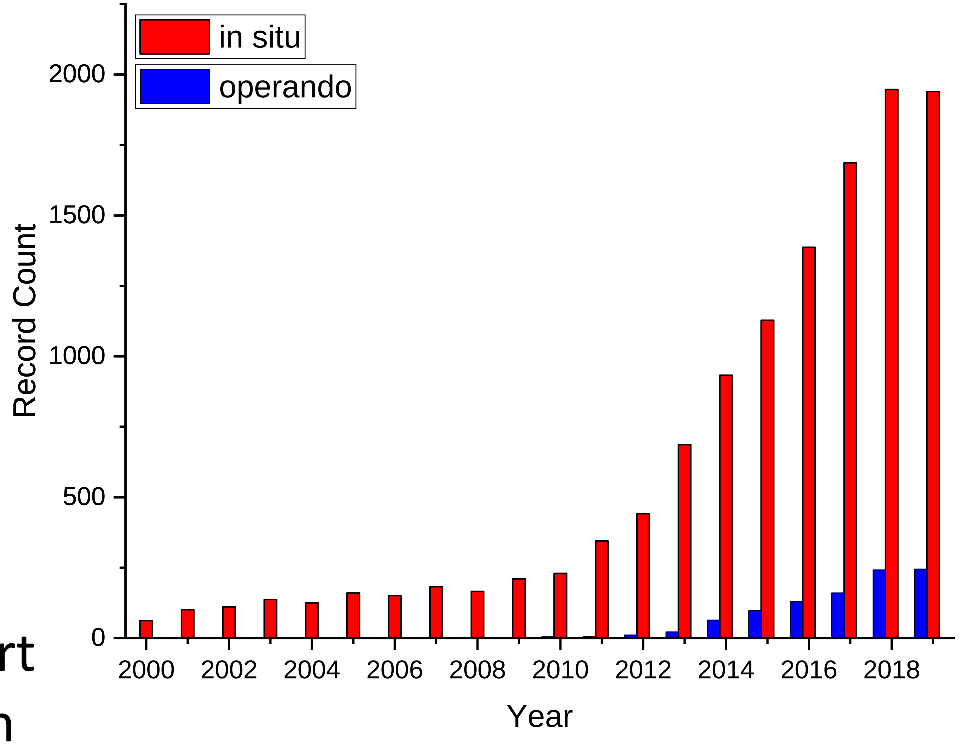

Web of Science November 2019

Center for Mesoscale Transport Properties

http://stonybrook.edu/m2m

Mission: To understand and ultimately control transport properties in complex battery systems with respect to multiple length scales

To build the scientific knowledge to enable creation of *scalable* electrochemical energy storage systems through fundamental understanding of transport properties.

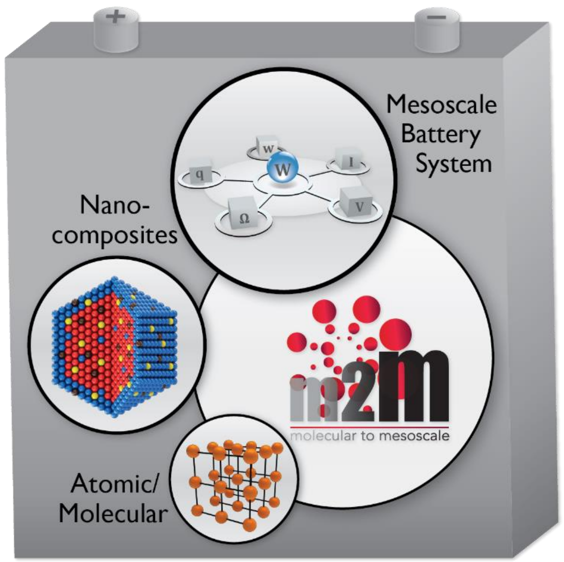

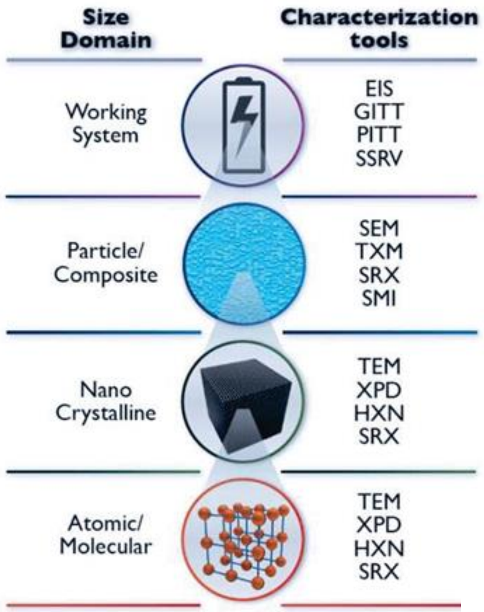

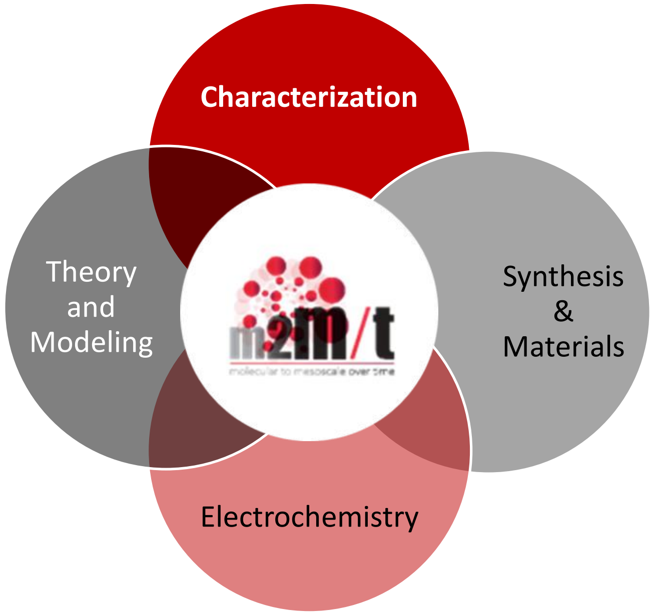

Investigation over Mutliple Length Scales

Charge transfer (ion and electron) must be considered over *multiple length scales*:

atomic/molecular, crystallite, particle/aggregate, electrode, system.

Beneficial insights are gained by using multiple probes of the system.

Two main types of active materials:

ion insertion materials - small structural rearrangement

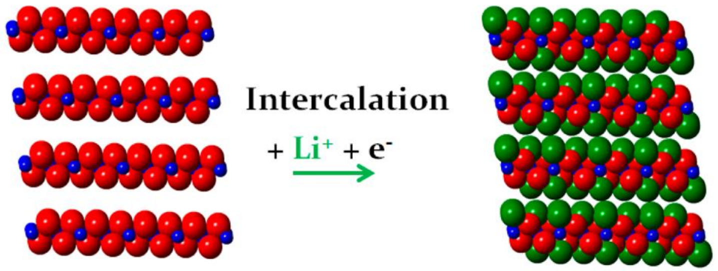

conversion materials - high capacity

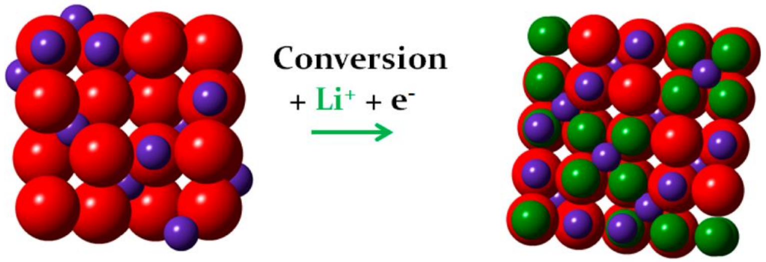

P. F. Smith, K. J. Takeuchi, A. C. Marschilok, E. S. Takeuchi, "Holy Grails in Chemistry: Investigating and Understanding Fast Electron/Cation Coupled Transport within Inorganic Ionic Matrices," Special Issue: *Accounts Chem Res.*, **2017**, *50,* 544−548. *Invited.*

Magnetite: Fe_3O_4 High Capacity Conversion Material

high energy density ↑
environmentally sustainable material ↑
multiple electron transfers (8!) per Fe_3O_4 formula unit ↑

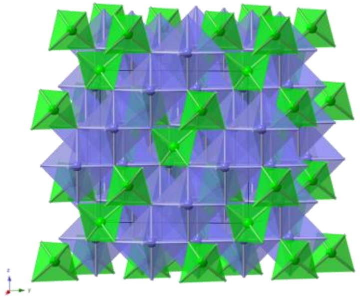

$Fe_3O_4 + Li^+ + e^- \rightarrow LiFe_3O_4$

$LiFe_3O_4 + Li^+ + e^- \rightarrow Li_2Fe_3O_4$

$Li_2Fe_3O_4 \rightarrow 3FeO + Li_2O$

$FeO + 2Li^+ + 2e^- \rightarrow Fe^0 + Li_2O$

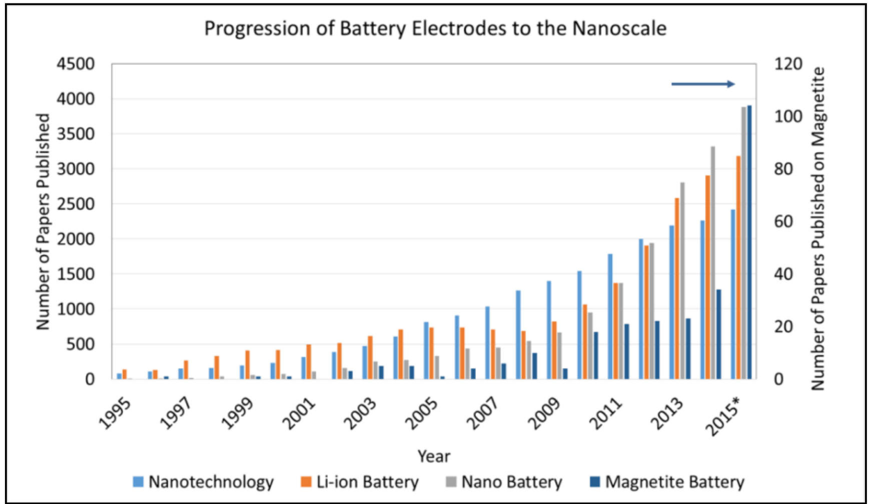

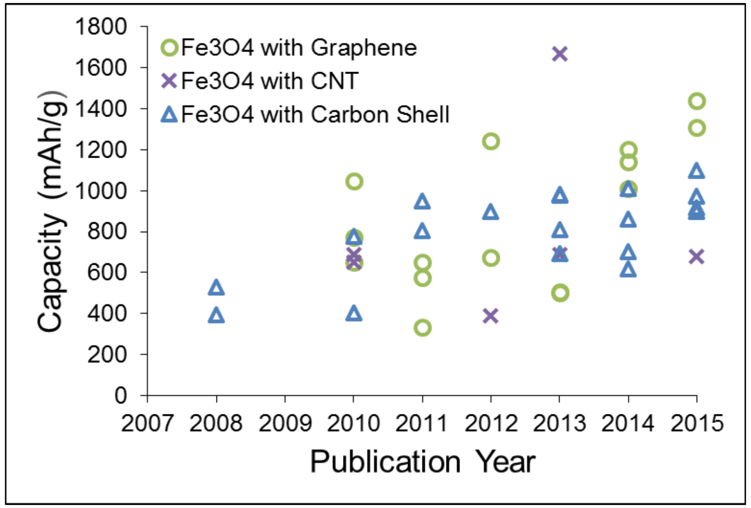

M. Thackeray, W. David, J. Goodenough, *J. Mater. Res. Bull.*, **1982**, 17, 785.
A. Bruck, C. Cama, C. Gannett, A. Marschilok, E. Takeuchi, K. Takeuchi, *Inorg. Chem. Front.*, **2016,** *3,* 26. *invited review.*
A. Abraham, L. Housel, C. Lininger, D. Bock, J. Jou, F. Wang, A. West, A. Marschilok, K. Takeuchi, E. Takeuchi, *ACS Cent. Sci.*, **2016,** *2(6),* 380.

Structure-determined ionic transport in Fe_3O_4

Detailed lithiation process revealed, with FeO formation and ccp-O framework retention.

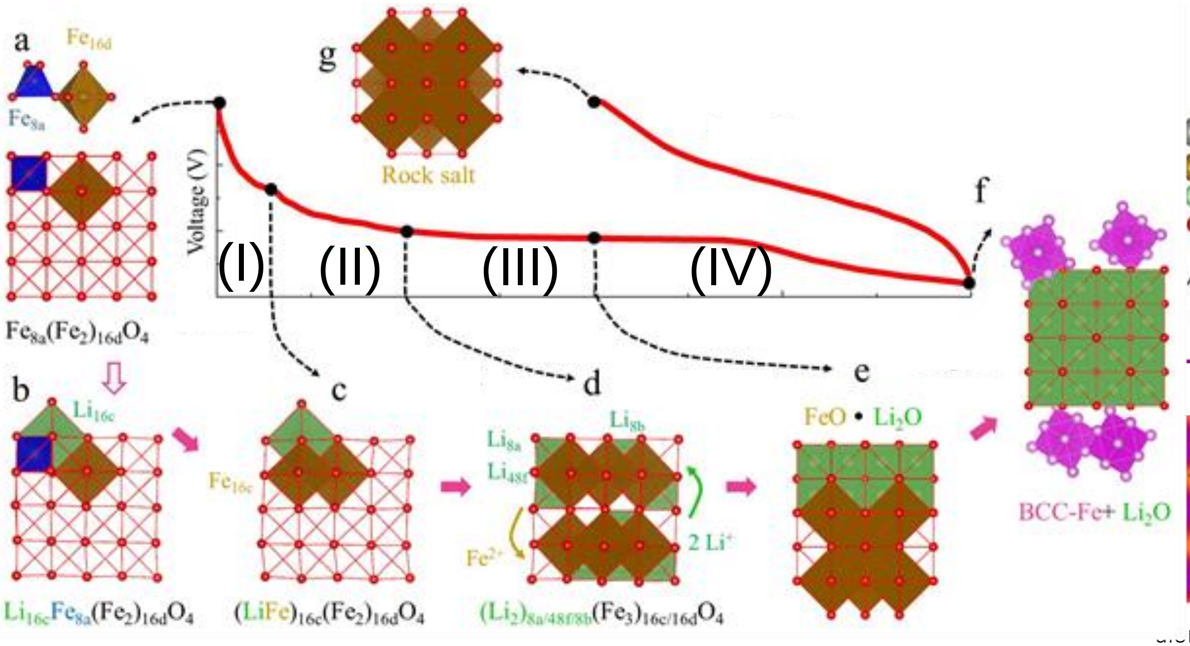

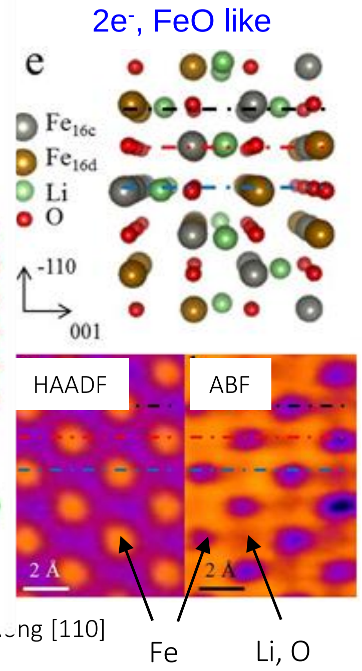

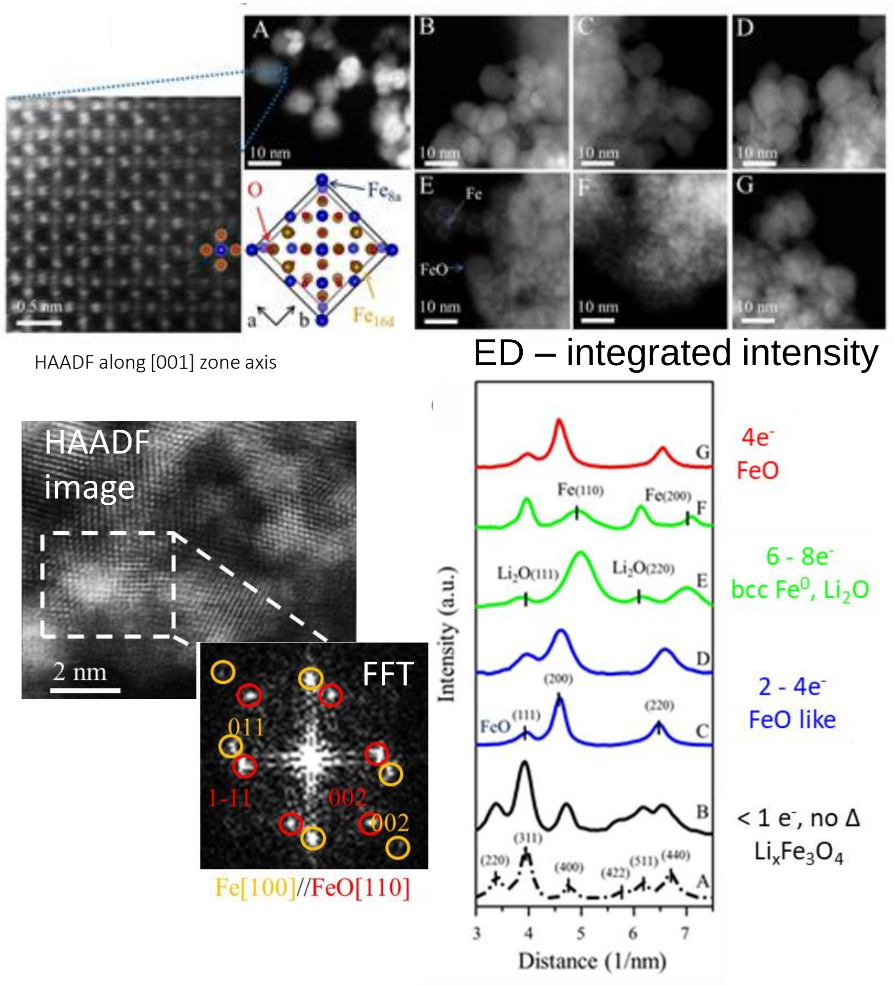

(I-II) DFT+U predicted $Li_2Fe_3O_4$ structure preserves O-anion framework with 15% vol. expansion, in agreement with EXAFS.

(III-IV) HAADF showed coherent Fe-FeO orientation.

W. Zhang, D. Bock, C. Pelliccione, Y. Li, L. Wu, Y. Zhu, A. Marschilok, E. Takeuchi, K. Takeuchi, F. Wang, *Adv. Energy Mat.*, **2016,** *6(10),* 1502471.

In-situ Electron Diffraction and Atomic Imaging Reveal Ionic transport pathways during topotactic reaction

Single-crystal e-diffraction

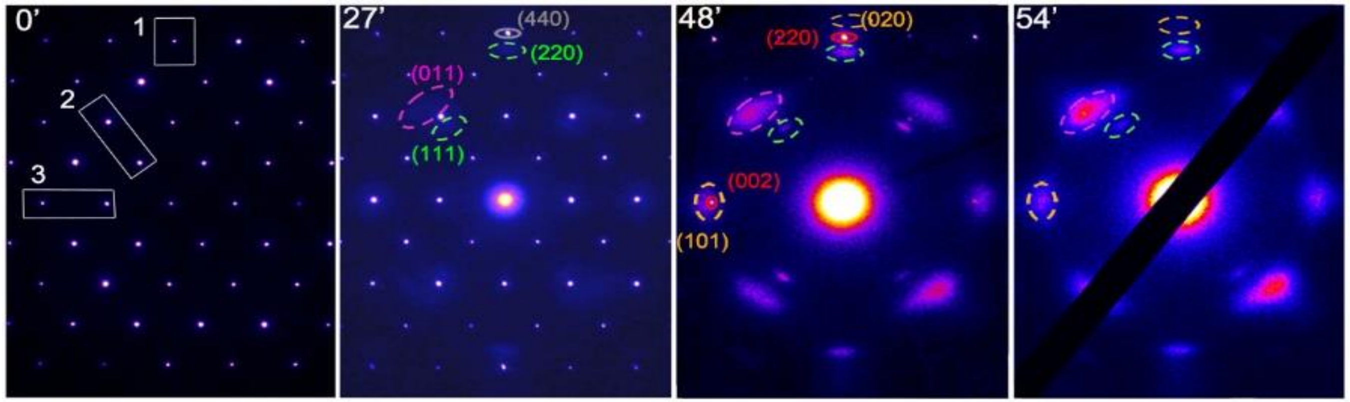

Integrated intensity

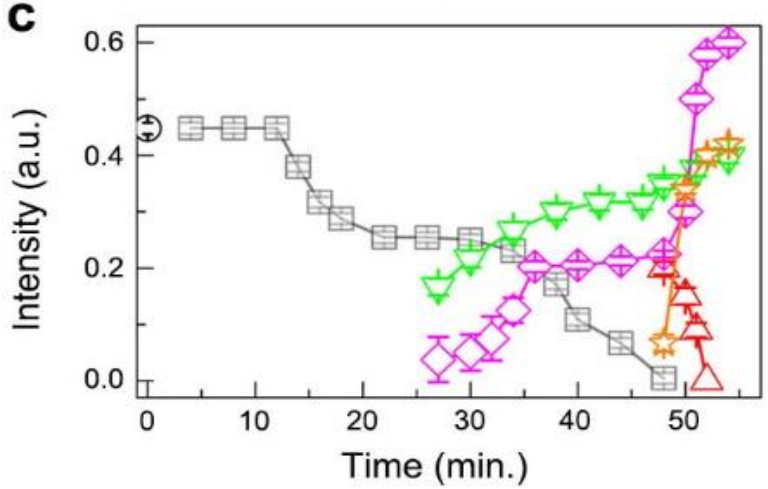

Intensity plots

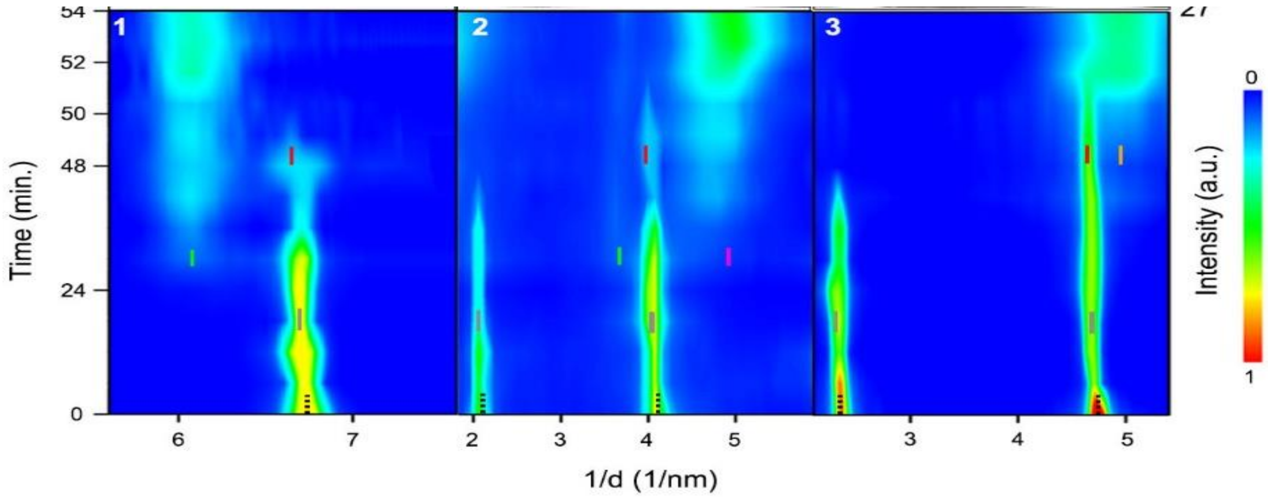

Lattice change

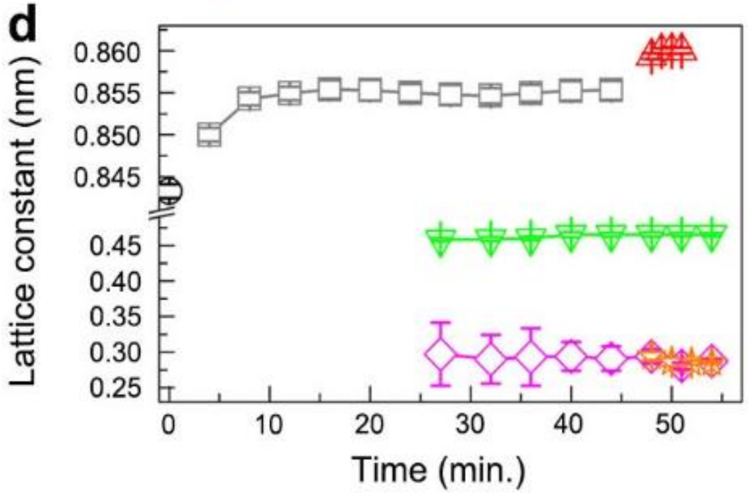

W. Zhang, Y. Li, Y. Duan, L. Wu, K. Kisslinger, C. Chen, D.C. Bock, P. Pan, Y. Zhu, A.C. Marschilok, E.S. Takeuchi, K. J. Takeuchi, F. Wang, *Nat. Commun.*, **2019,** *10,* 1972.

Size significantly impacts ion transport and functional capacity

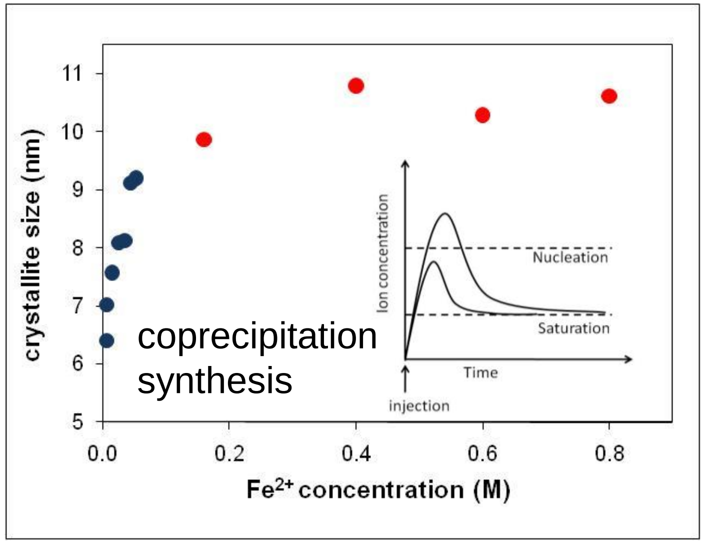

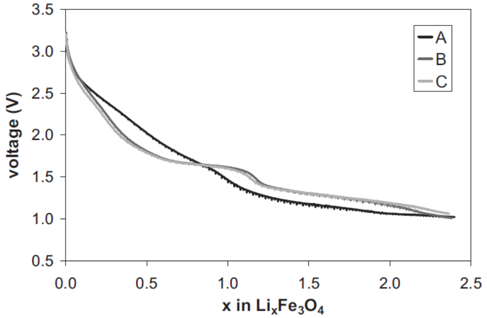

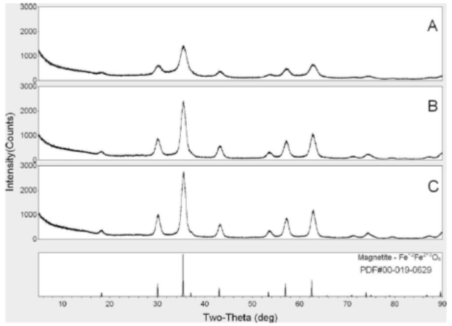

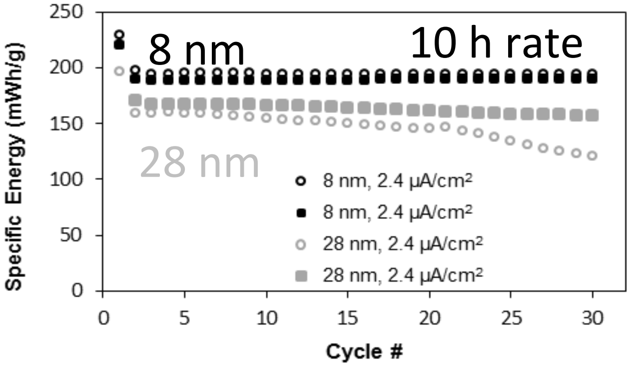

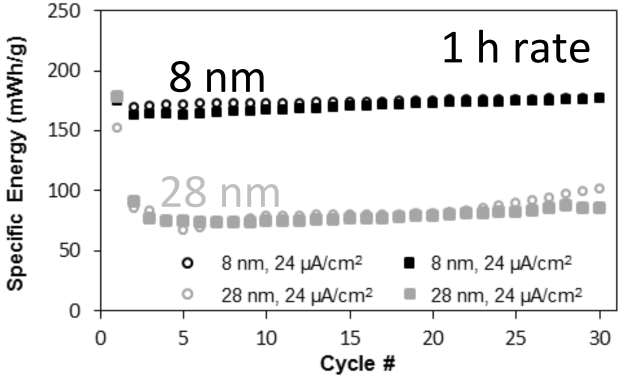

Fe_3O_4 electrode

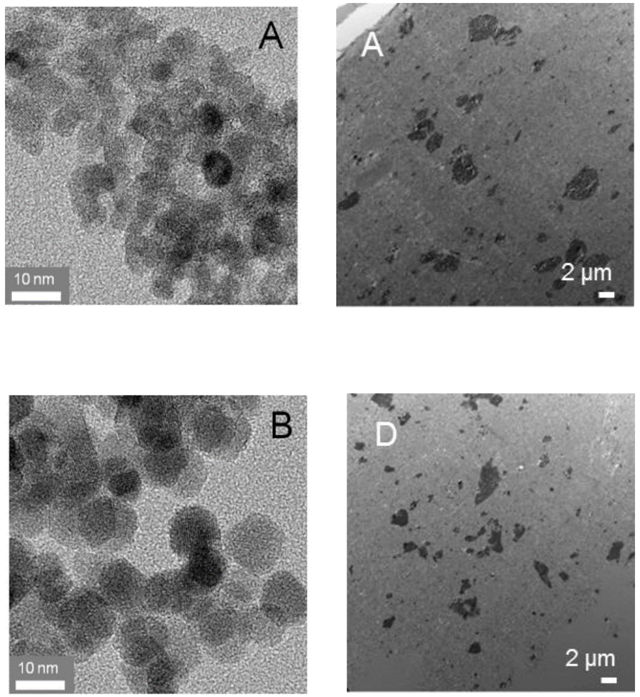

8 nm

28 nm

S. Zhu, A. Marschilok, E. Takeuchi, G. Yee, G. Wang, K. Takeuchi, *Electrochem. S.S. Lett.*, **2009,** *12(4),* A91.

S. Zhu, A. Marschilok, E. Takeuchi, G. Yee, G. Wang, K. Takeuchi, *J. Electrochem. Soc.* **2010**, *157*, A1158.

D.C. Bock, K.C . Kirshenbaum, J. Wang, W. Zhang, F. Wang, J. Wang, A.C. Marschilok, K.J. Takeuchi, E.S. Takeuchi, *ACS Appl. Mater. Interfaces* **2015**, *7(24),* 13457.

W. Zhang, D. Bock, C. Pelliccione, Y. Li, L. Wu, Y. Zhu, A. Marschilok, E. Takeuchi, K. Takeuchi, F. Wang, *Adv. Energy Mat.*, **2016,** *6(10),* 1502471.

Multiscale Continuum Model Affirms Importance of Size

Consideration of both crystallite and aggregate sizes was necessary to describe diffusion during load (V) and relaxation (ΔV_{max}).

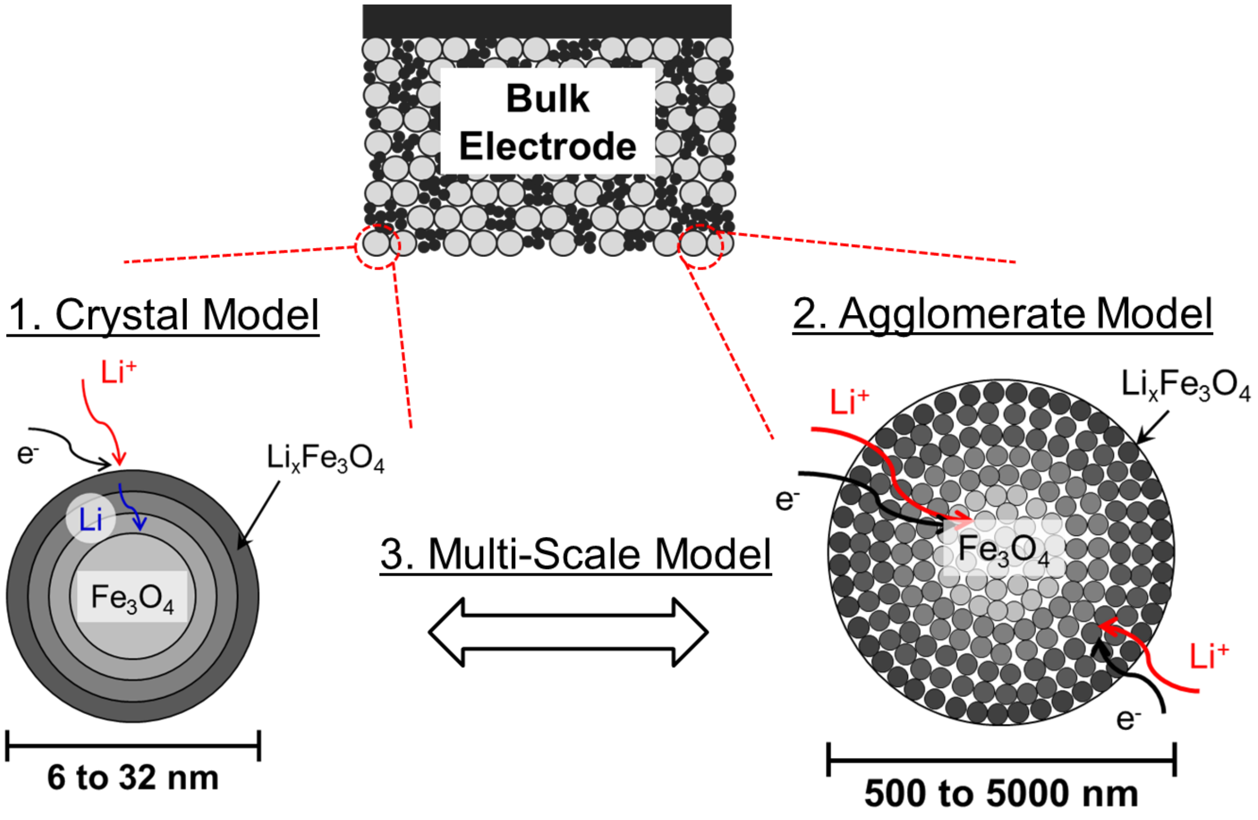

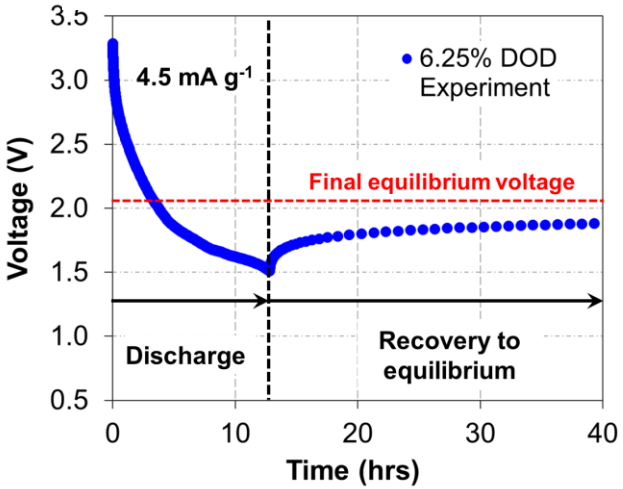

Governing Equations

Mass (agg.)
$$\varepsilon \frac{\partial c_{agg}}{\partial t} = \varepsilon D_{agg}\frac{\partial^2 c_{agg}}{\partial r^2} + \frac{2\varepsilon D_{agg}}{r}\frac{\partial c_{agg}}{\partial r} + \frac{a i_{rxn}}{F}$$

Fickian diffusion

Mass (crystal)
$$\frac{\partial c_x}{\partial t} = D_x \frac{\partial^2 c_x}{\partial \bar{r}^2} + \frac{2D_x}{\bar{r}}\frac{\partial c_x}{\partial \bar{r}}$$

Butler-Volmer

Reaction
$$i_{rxn} = i_0\left[\exp\left(\frac{\alpha_a F(\varphi_1 - U)}{R_G T}\right) - \exp\left(\frac{-\alpha_c F(\varphi_1 - U)}{R_G T}\right)\right]$$
$$i_0 = F k_{rxn} c_{agg}^{\alpha_a} c_x^{\alpha_c} \left(c_{x,max} - c_x\right)^{\alpha_a}$$

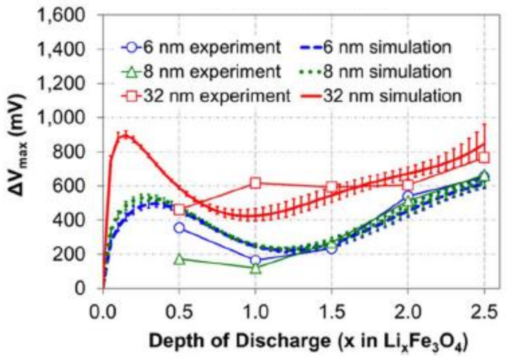

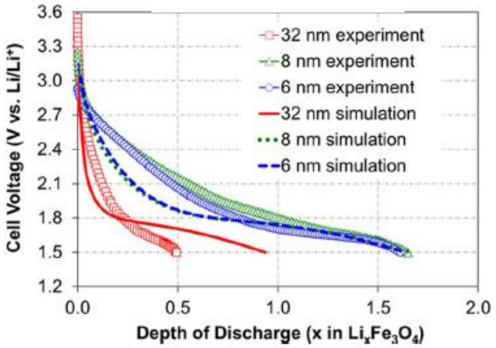

K. Knehr, N. Brady, C. Cama, D. Bock, Z. Lin, C. Lininger, A. Marschilok, K. Takeuchi, E. Takeuchi, A. West, *J. Electrochem. Soc.*, **2015,** *162,* A2817.

Operando Isothermal Microcalorimetry

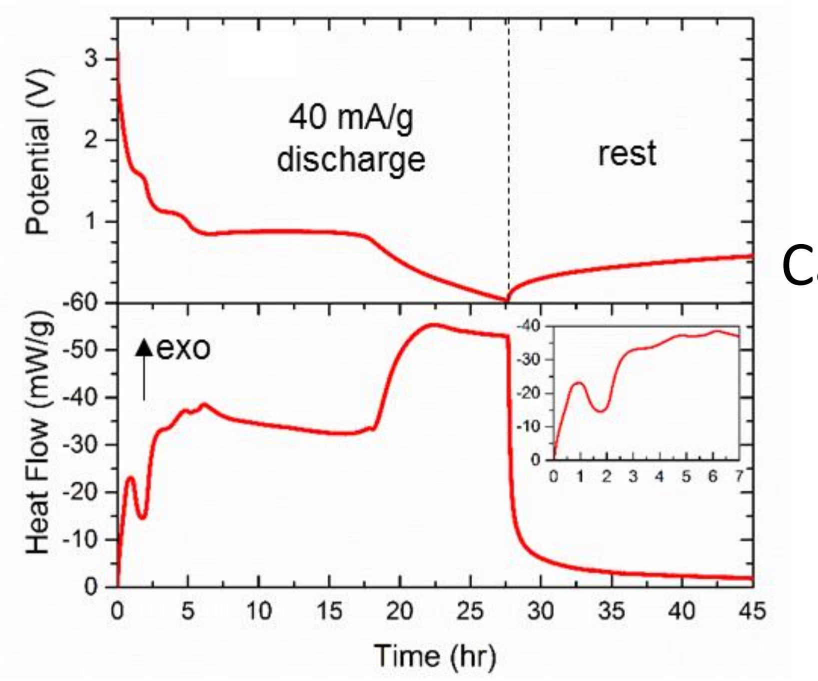

Total Reaction

$$Fe_3O_4 + 8Li \rightarrow 3Fe^0 + 4Li_2O$$

Capacity and heat dissipation > predicted values

Theoretical Heat

$$\Delta H_{rxn} = \sum_i v_i \Delta H_{f,i}$$

$$\Delta S_{rxn} = \sum_i v_i \Delta S_{f,i}$$

Measured Heat

$$\Delta H = Q - W$$

$$Q = Heat\ from\ calorimeter$$

$$W = Electrical\ Work$$

Capacity (Li equivalents)	ΔG_{rxn} (J/g)= ΔH_{rxn}-T ΔS_{rxn}
8.0	-5508

Theoretical

Capacity (Li equivalents)	ΔH_T (J/g)
9.6	-7261

Observed

M. Huie, D. Bock, L. Wang, A. Marschilok, K. Takeuchi, E. Takeuchi, *J. Phys. Chem. C*, **2018,** *122(19),* 10316-10326.

Operando IMC Comparison of 12 nm vs. 29 nm Fe_3O_4

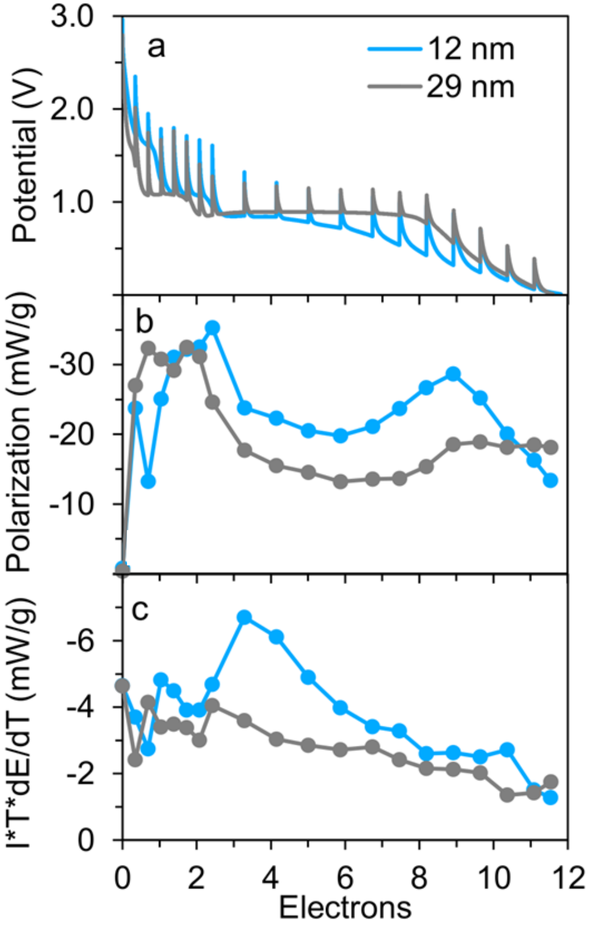

Contributions from Polarization and Entropic Heat

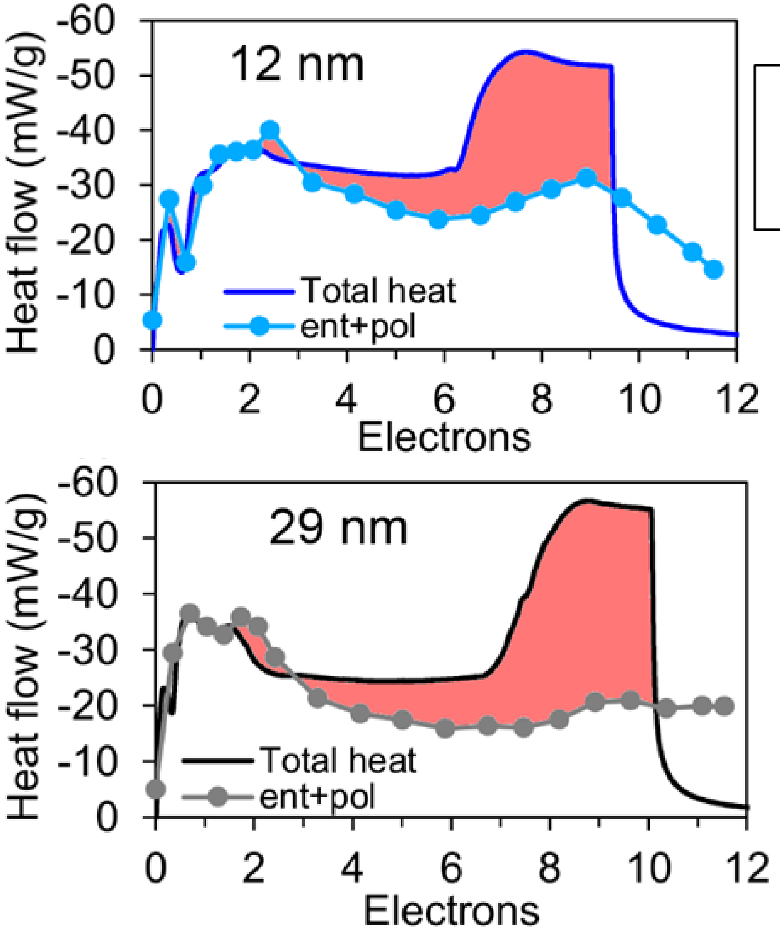

Comparison of Parasitic Heat (red)

$$\dot{Q} = I\left(E_{load} - E_{ocp}\right) + I\left(T\frac{dE_{ocp}}{dT}\right) + \dot{Q}_p$$

polarization

entropy

parasitic heat

Larger crystallite size (29 nm) Fe_3O_4 produces <u>more</u> parasitic heat

Crystallite Size (nm)	Total heat IMC (J/g)	Total heat predicted (J/g)	Parasitic Heat (J/g)
12	-4014	-2859	-1155
29	-3704	-2358	-1346

M.M. Huie, D.C. Bock, A.M. Bruck, K.R. Tallman, L.M. Housel, L. Wang, J. Thieme, K.J. Takeuchi, E. Takeuchi, A. Marschilok, *ACS Applied Mater. Inter.*, **2019,** *11(7),* 7074-7086.

Operando Xray Absorption Spectroscopy (XAS)

Operando XAS provides insight on:

Average oxidation state

Structure and coordination environment

Microfluorescence mapping determines electyrochemical activity as influenced by local environment.

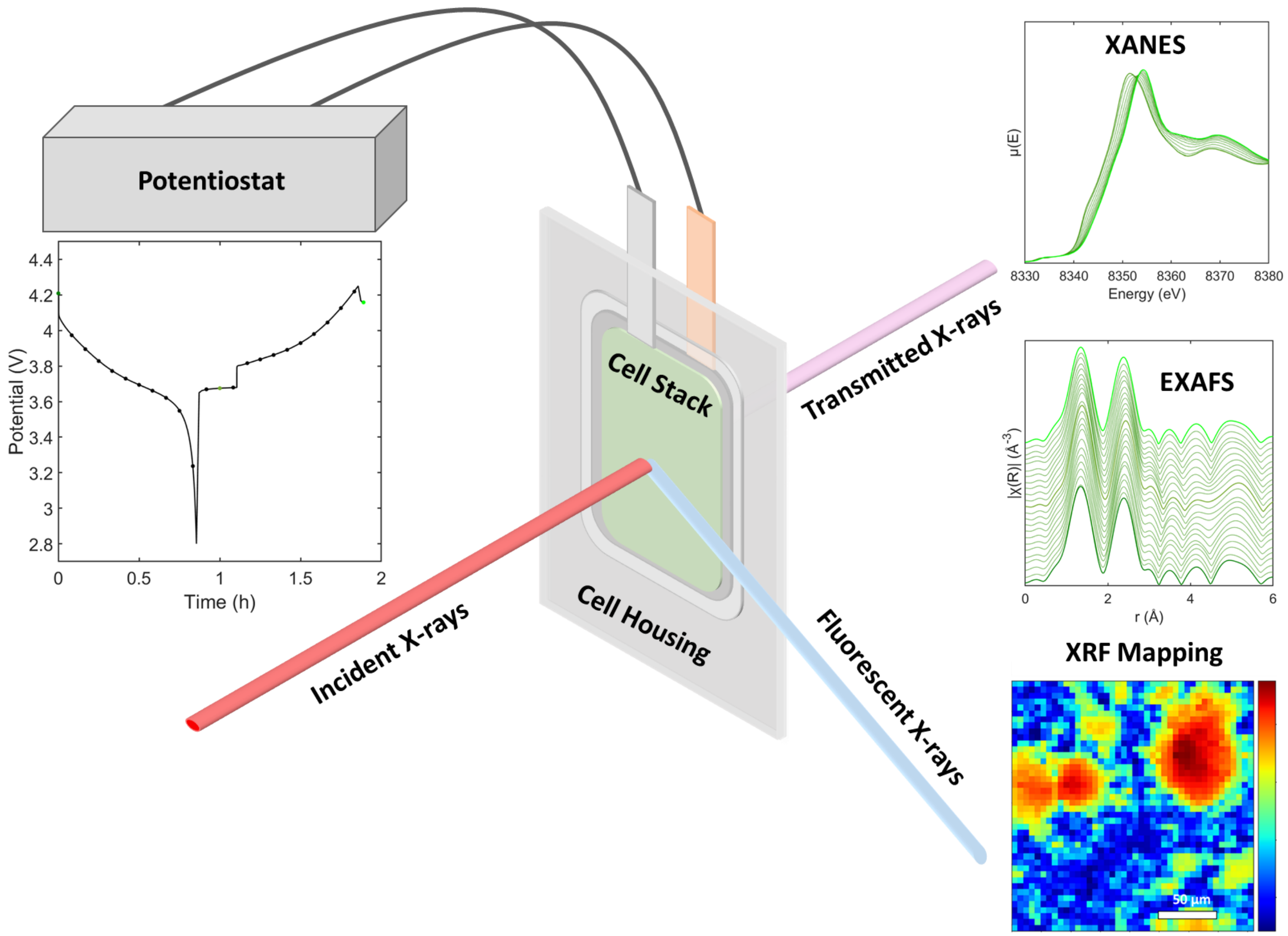

Operando XAS Measurements of Lithiation

Good agreement between model and XAS up to ~2 e^- equivalents.
Deviation at higher lithiation consistent with heat generation and SEI formation.

***In-situ* EXAFS**

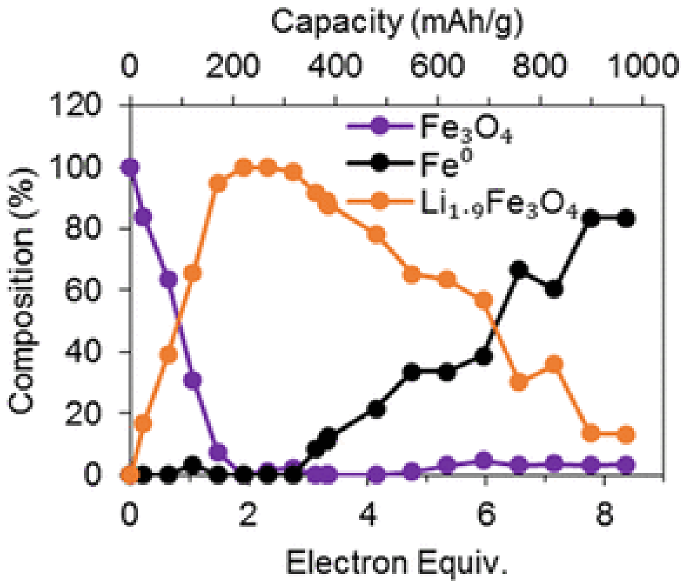

***In-situ* XANES**

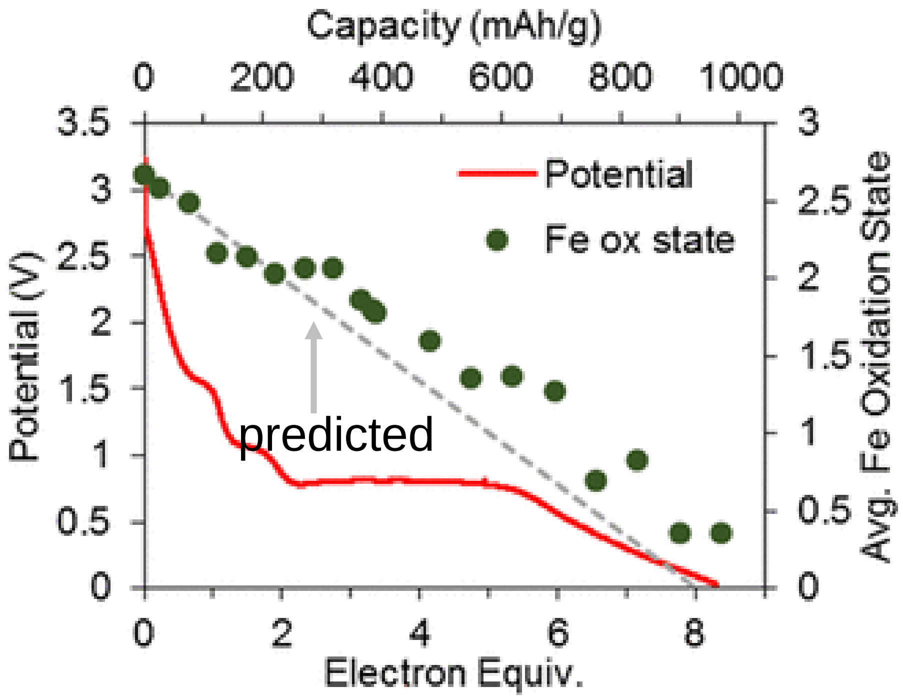

***In-situ* XAS**

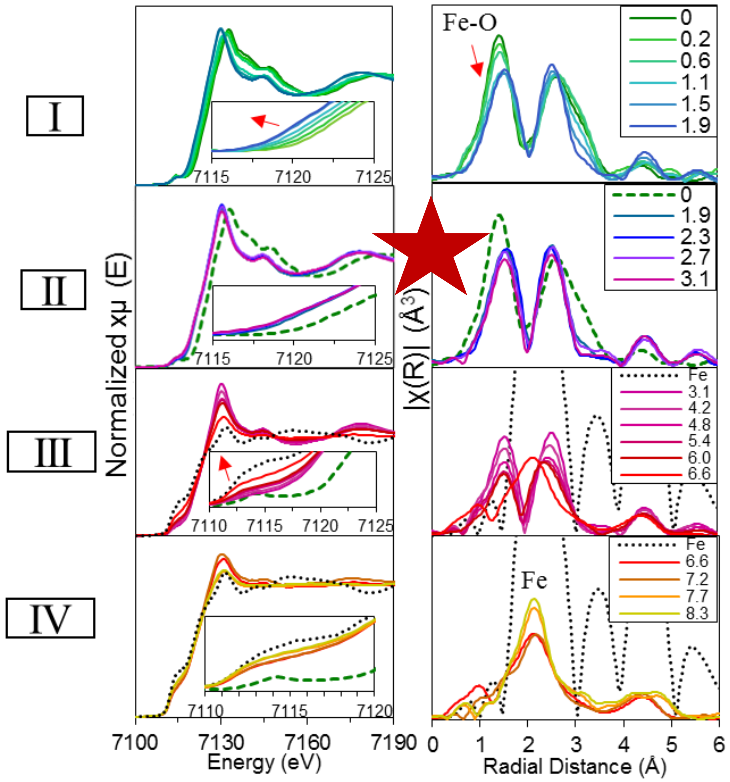

NSLS II

M. Huie, D. Bock, L. Wang, A. Marschilok, K. Takeuchi, E. Takeuchi, *J. Phys. Chem. C*, **2018,** *122(19),* 10316-10326.

Reactions Observed during Lithiation

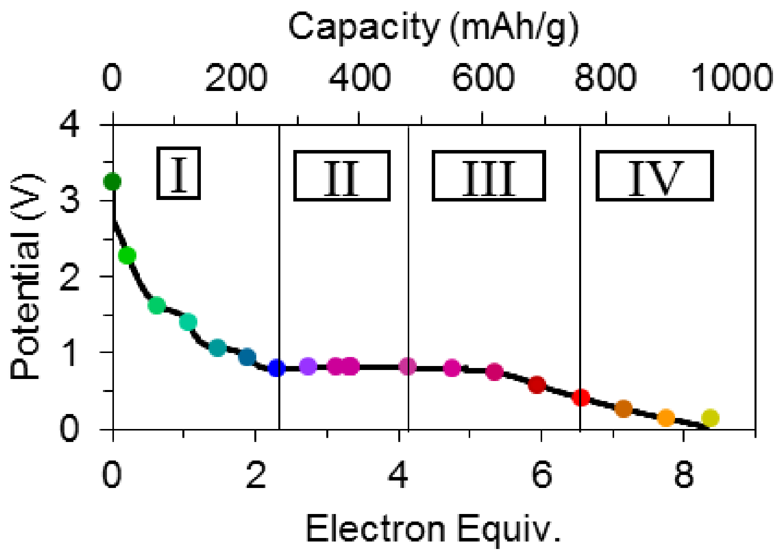

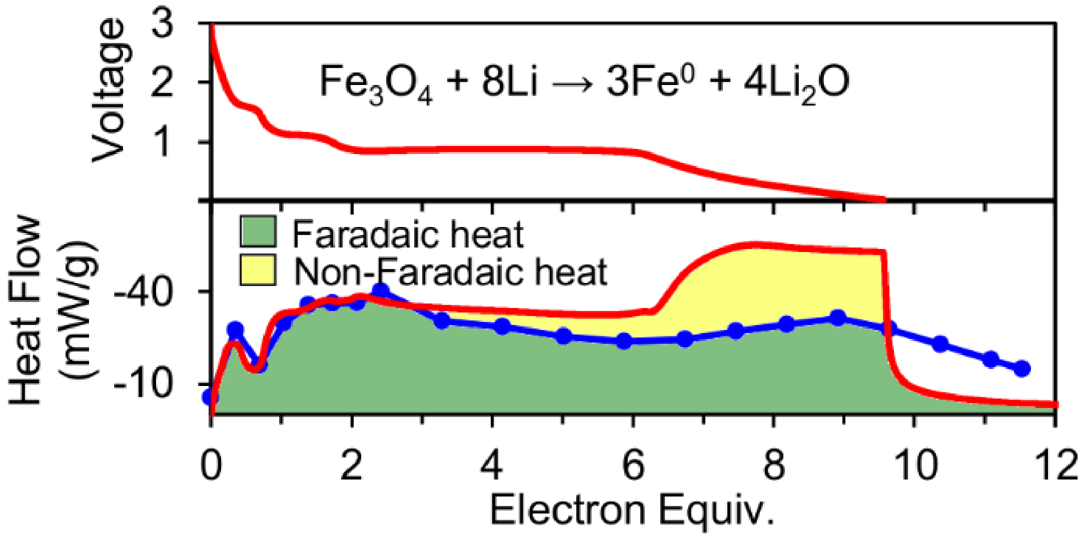

I $$Fe_3O_4 + 2Li^+ + 2e^- \rightarrow Li_2Fe_3O_4$$

II Onset Electrolyte Reduction

III $$Li_2Fe_3O_4 + 2Li^+ + 2e^- \rightarrow 2Li_2O + 2FeO + Fe^0$$

IV $$2FeO + 4Li^+ + 4e^- \rightarrow 2Li_2O + 2Fe^0$$

$$Fe_3O_4 + 8Li^+ + 8e^- \rightarrow 3Fe^0 + 4Li_2O$$

M. Huie, D. Bock, L. Wang, A. Marschilok, K. Takeuchi, E. Takeuchi, *J. Phys. Chem. C*, **2018,** *122(19),* 10316-10326.

Operando Spatially Resolved XAS

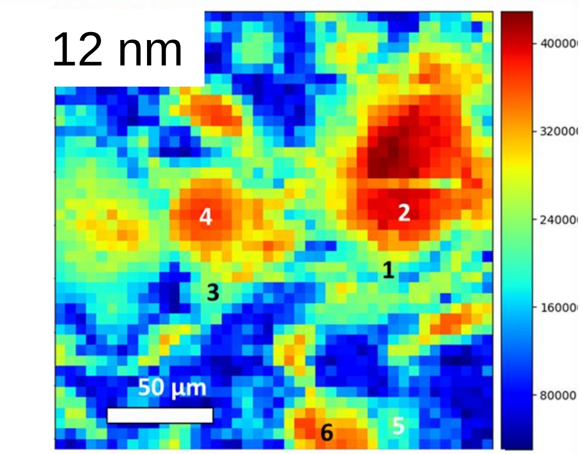

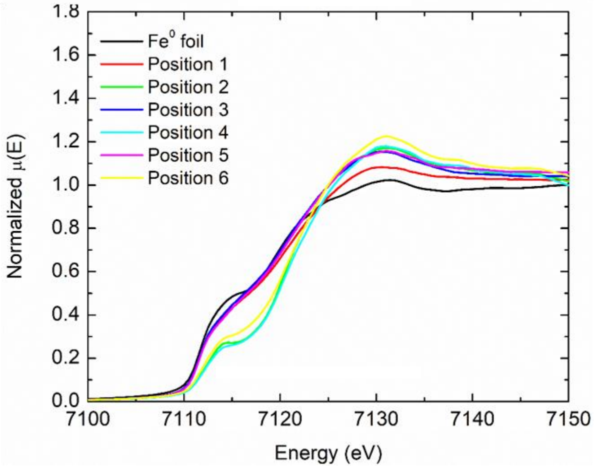

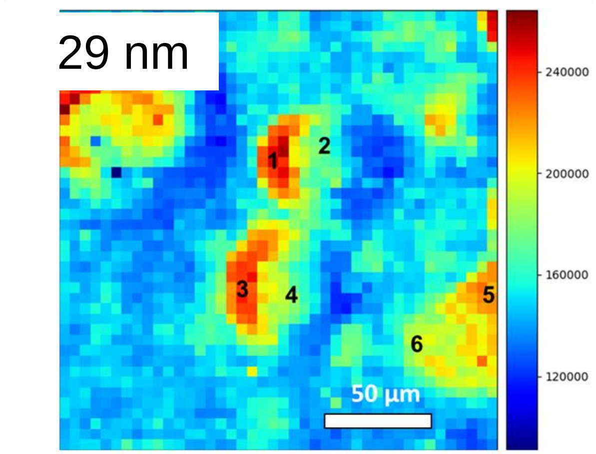

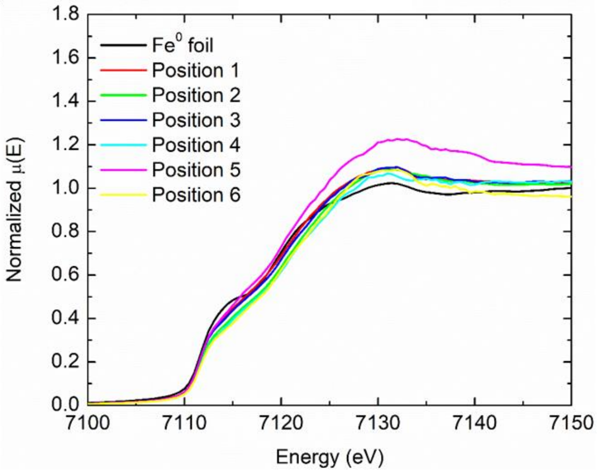

At C/2 rate, discharge inhomogeneity in 12 nm Fe_3O_4 agglomerates, can be detected by a mapping coupled with localized XANES measurement. Lack of full electrochemical reduction to Fe^0 in agglomerate center.

Position # from XRF map	Average oxidation state from LCF fit			
	12 nm C/10	12 nm C/2	29 nm C/10	29 nm C/2
Position 1 (edge)	0.4 ± 0.1	0.2 ± 0.1	0.2 ± 0.1	0.2 ± 0.1
Position 2 (center)	0.4 ± 0.1	1.2 ± 0.1	0.1 ± 0.2	0.4 ± 0.1
Position 3 (edge)	0.5 ± 0.1	0.1 ± 0.1	0.2 ± 0.2	0.2 ± 0.1
Position 4 (center)	0.4 ± 0.1	1.2 ± 0.1	0.1 ± 0.2	0.4 ± 0.1
Position 5 (edge)	-	0.2 ± 0.1	-	0.4 ± 0.2
Position 6 (center)	-	1.1 ± 0.1	-	0.5 ± 0.1

M.M. Huie†, D.C. Bock †, A.M. Bruck, K.R. Tallman, L.M. Housel, L. Wang, J. Thieme, K.J. Takeuchi, E. Takeuchi, A. Marschilok, *ACS Applied Mater. Inter.*, **2019,** *11(7),* 7074-7086.

Tracking Lithiation in thick Fe_3O_4 electrodes – Spatial Resolution

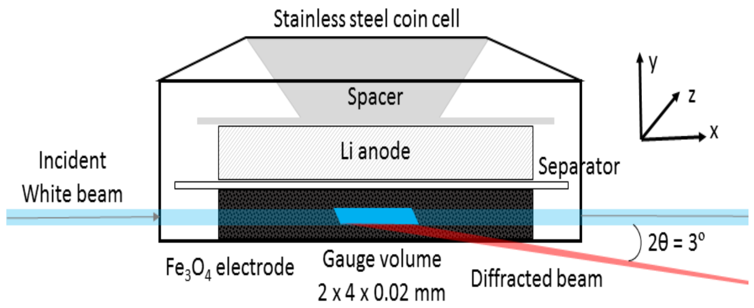

500 micron thick Fe_3O_4 electrodes

Energy Dispersive X-ray Diffraction (EDXRD)
Small (20 µm) white beam high energy x-ray.
Standard cells with no modification used.
Cell moved to probe various locations of cell.

Li/Fe_3O_4 cells measured *in situ.*
Ex-situ synchrotron ADXRD data also acquired for detailed refinement.

Pristine cell

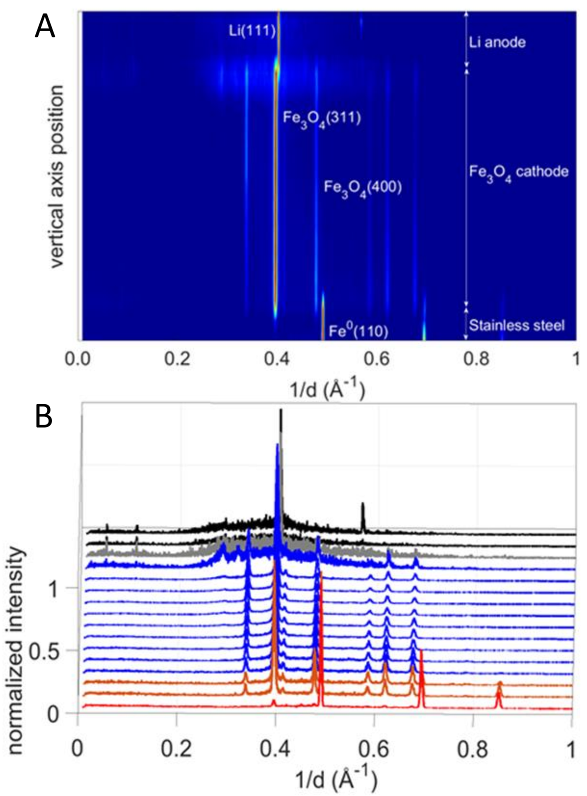

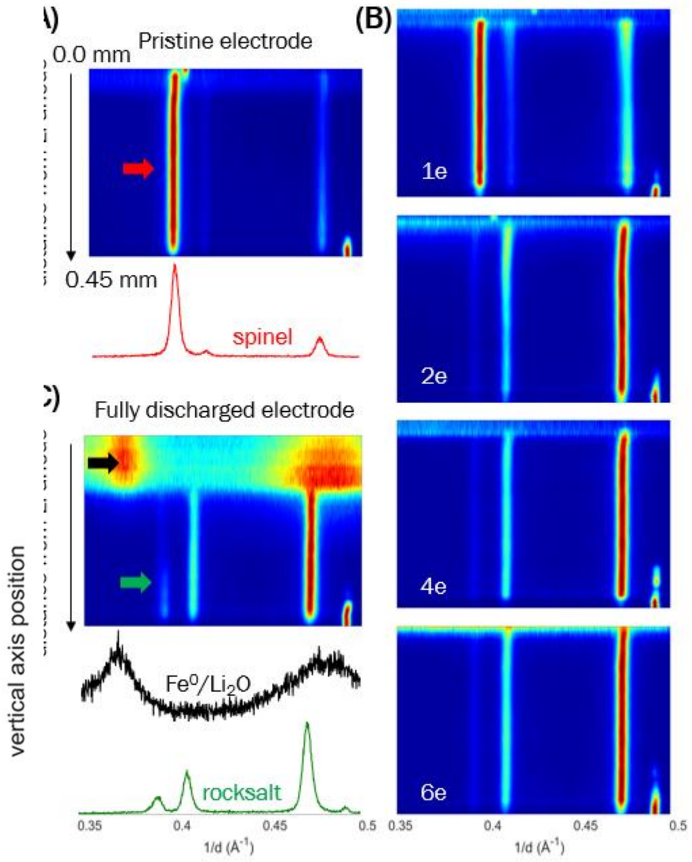

A.M. Bruck†, N.W. Brady†, C.N. Lininger, D.C. Bock, A.B. Brady, K.R. Tallman, C.D. Quilty, K.J. Takeuchi, E.S. Takeuchi, A.C. West, A.C. Marschilok, *ACS Appl. Energy Mater.*, **2019,** *2(4),* 2561.

Operando Cell

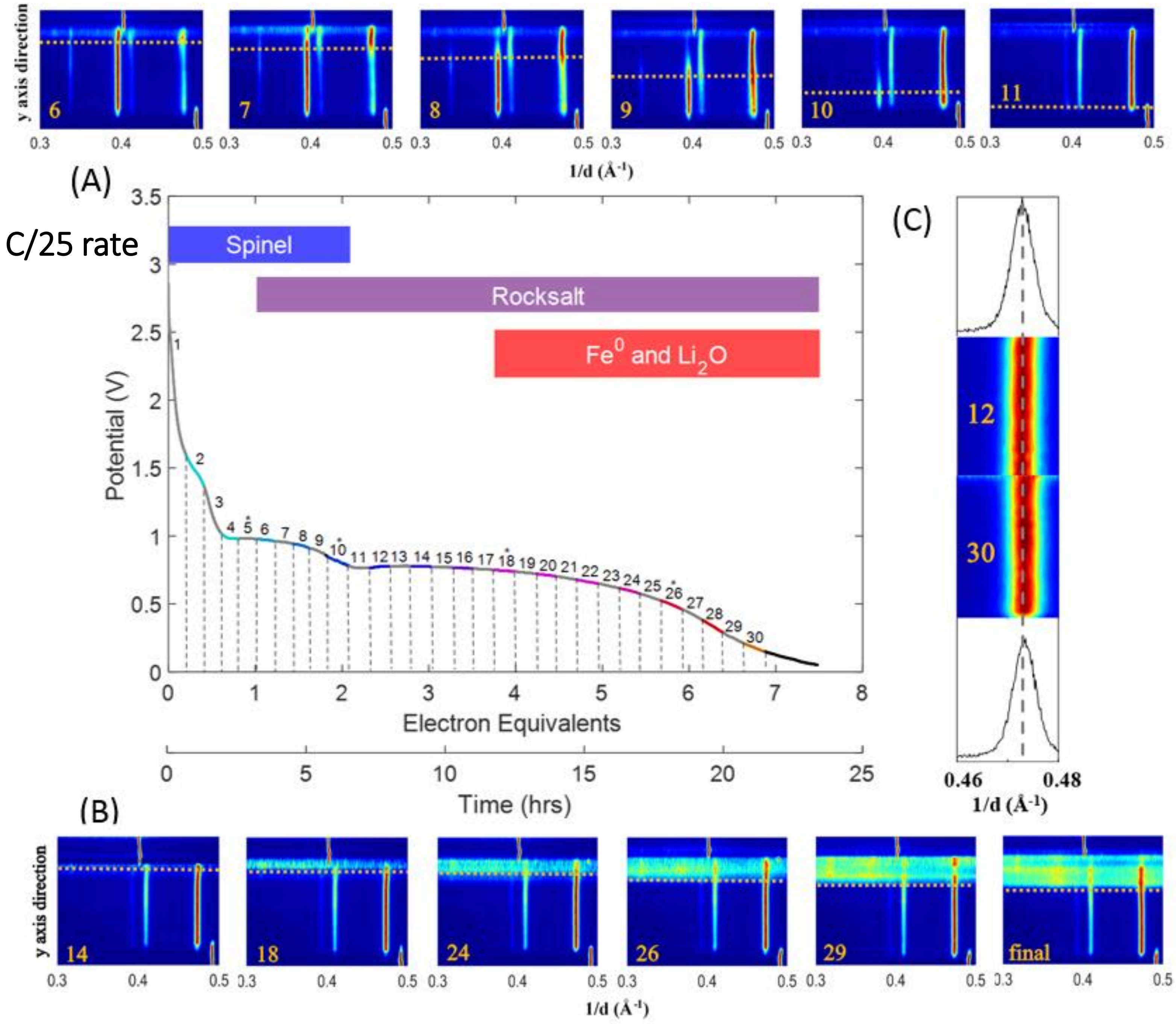

During initial Li^+ insertion, transformation to FeO rocksalt phase occurs in <2.3 electron equivalents

During conversion to Fe^0 and Li_2O, the electrochemical reaction propagates through the electrode until the lower discharge voltage limit is reached.

Li^+ diffusion through the electrode is the primary factor governing transport in the electrode.

Rocksalt observed through ~70% of the volume.

Fe^0 formation in ~30%

Operando Visualization of Electrochemical Activity Of 3-Dimensional Porous Electrode via EDXRD

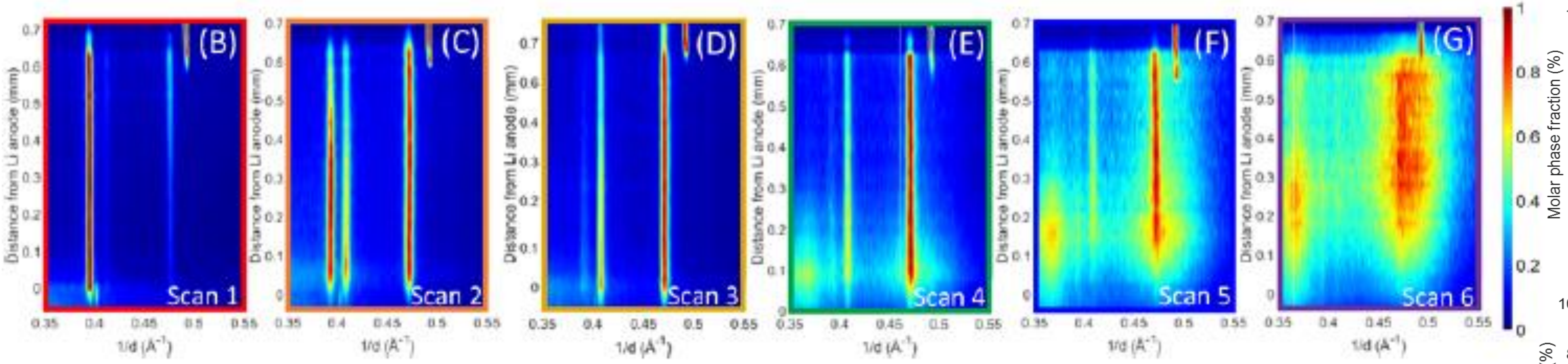

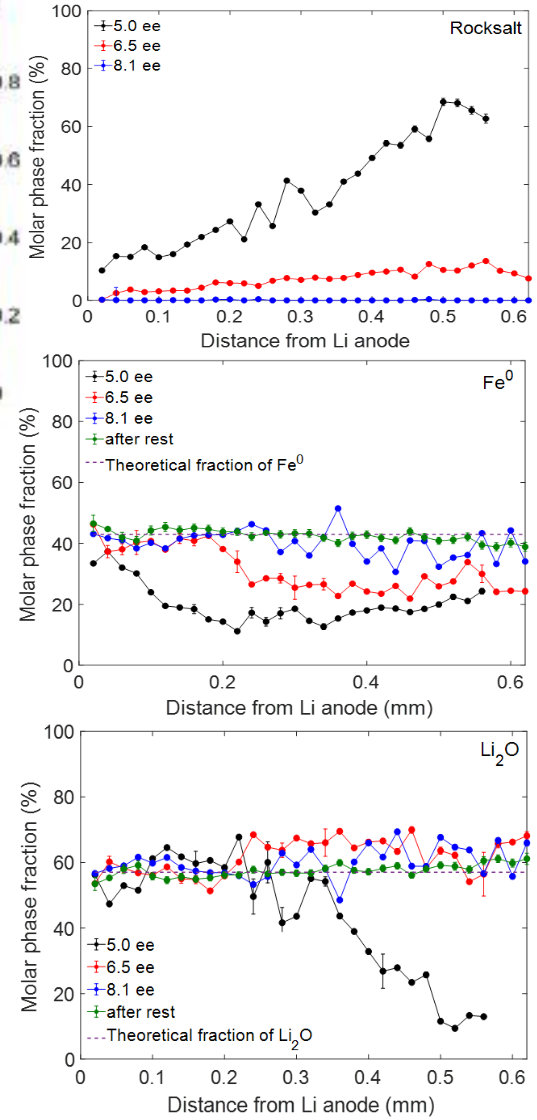

3D Porous electrodes enable ion access and electrochemical reaction throughout the entire ~500 µm thick electrode.

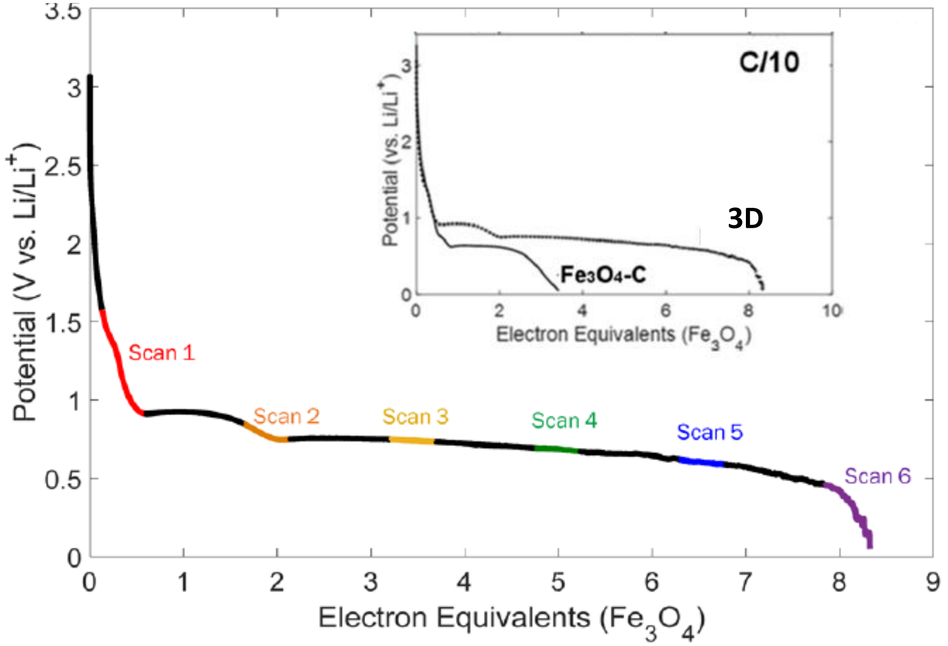

A.M. Bruck+, L. Wang+, A.B. Brady, D.M. Lutz, B.L. Hoff, K. Li, N. Stavinski, D.C. Bock, K.J. Takeuchi, E.S. Takeuchi, A.C. Marschilok, *J. Phys. Chem. C.*, **2019**, 123, 18834-18843.

Nonplanar 3-D Electrode Architectures for Ultrahigh Areal Capacity Batteries: Effect of Loading

Planar electrode

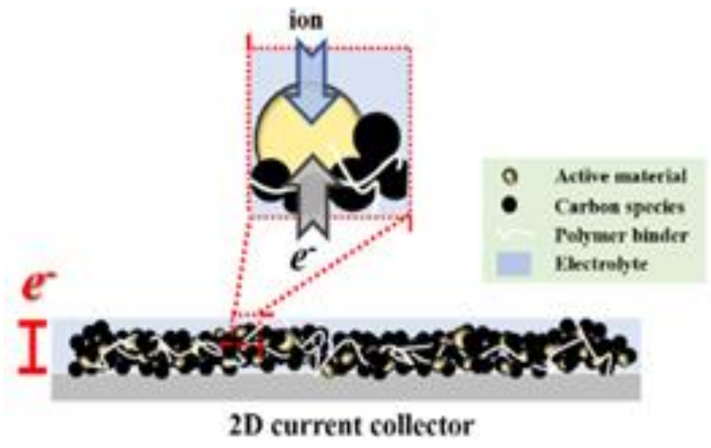

8 mg/cm²

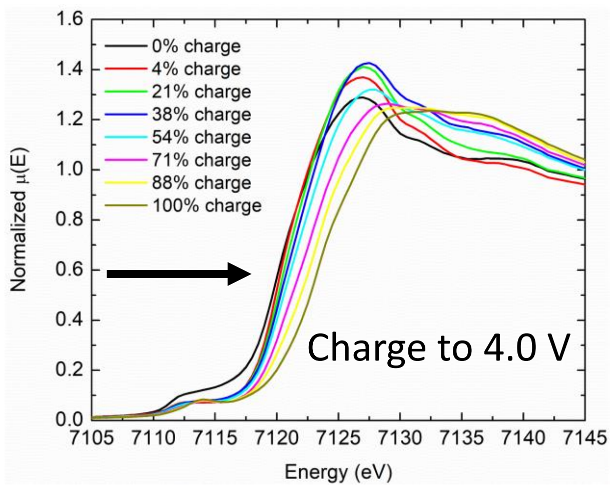

90 mg/cm²

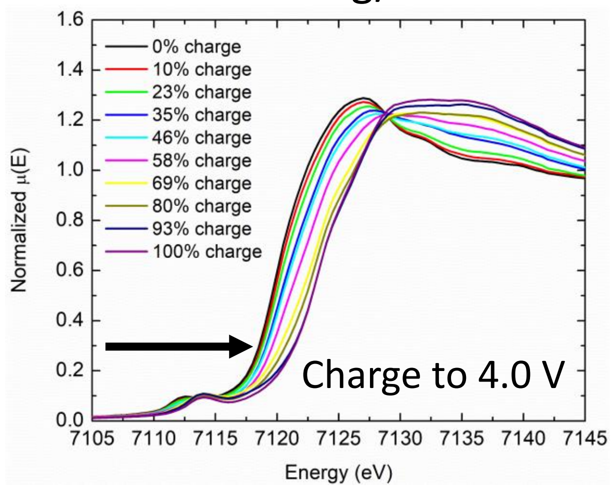

Nonplanar electrode

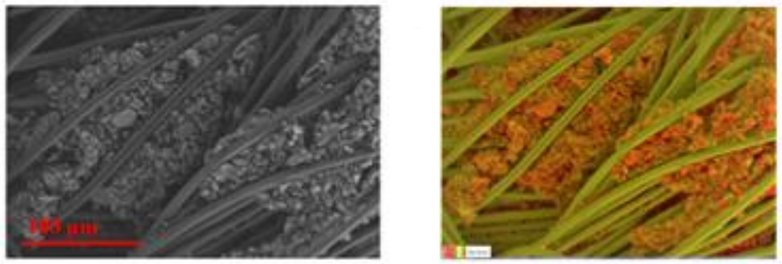

High loading electrodes are critical to achieving high energy density and pairing with high capacity anodes.

Operando XANES measurements performed on nonplanar $LiFePO_4$ (LFP) electrodes with low (8 mg/cm²) and high (90 mg/cm²) loading at C/4 charge rate.

J. Zheng, Q. Zhao, X. Liu, T. Tang, D.C. Bock, A.M. Bruck, K.R. Tallman, L.M. Housel, A.M. Kiss, A.C. Marschilok, E.S. Takeuchi, K.J. Takeuchi, L.A. Archer, L.A. *ACS Energy Lett.* **2019** 4, 1, 271-275.

Effect of Loading in Nonplanar Electrode Architectures for Ultrahigh Areal Capacity Batteries

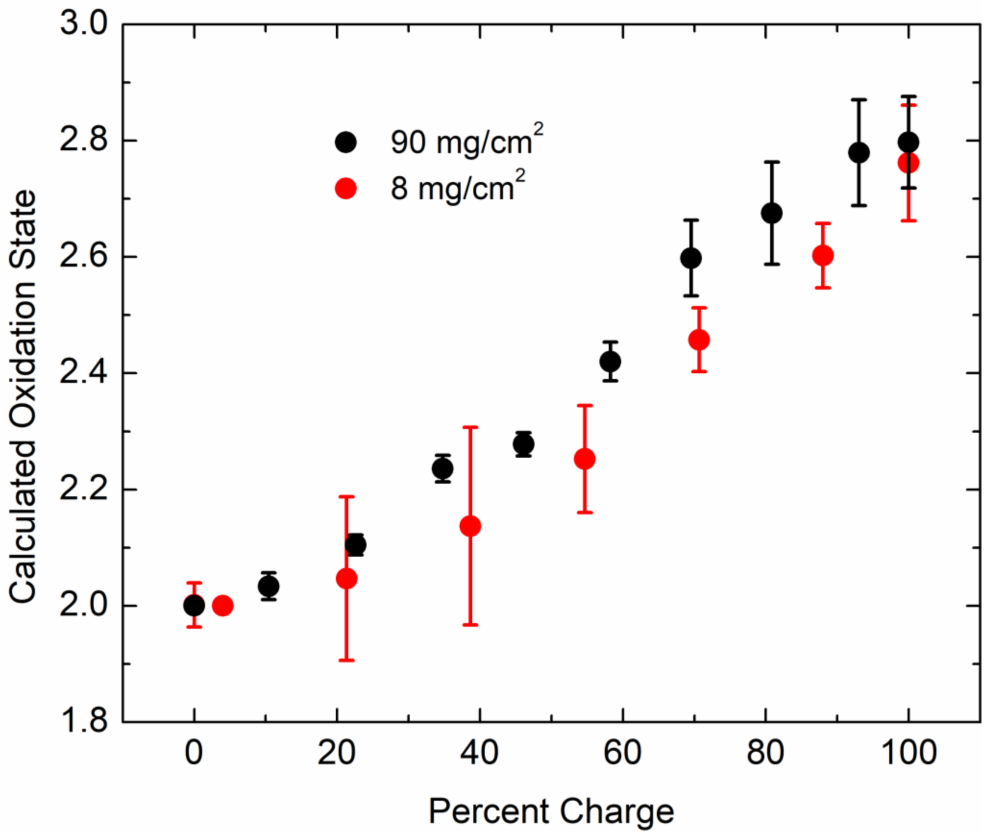

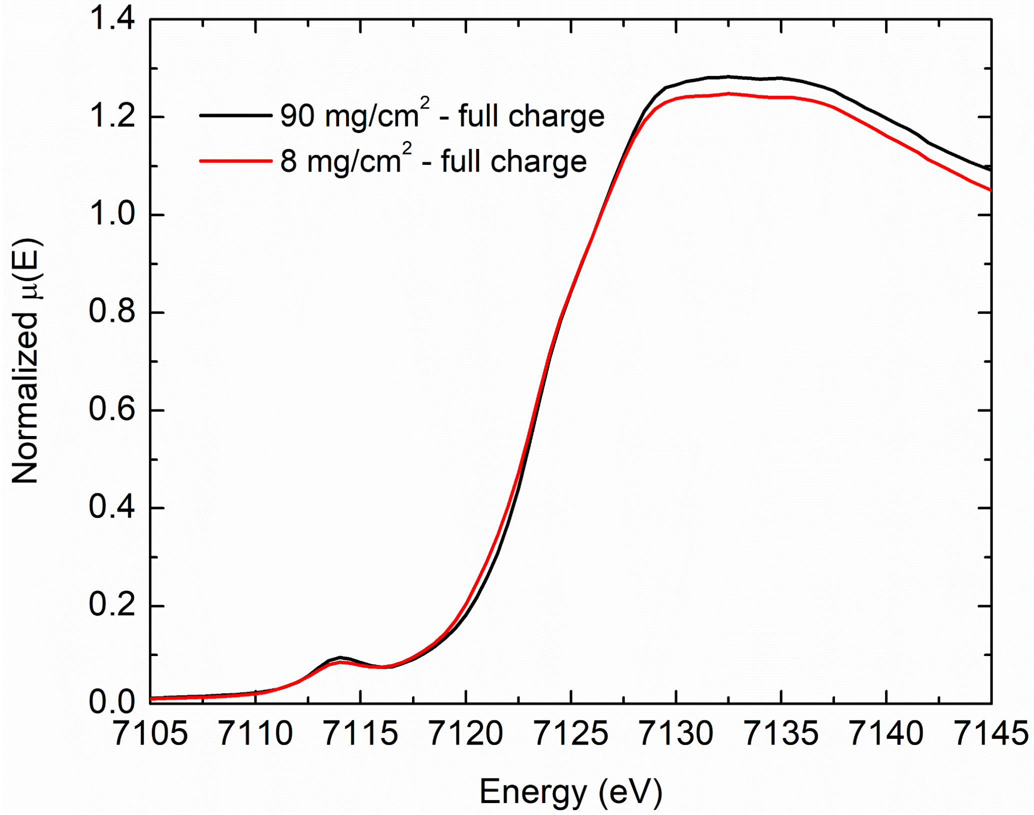

Equivalent edge position indicates both low loading (8 mg/cm^2) and high loading (90 mg/cm^2) nonplanar LFP electrodes were charged to the same oxidation state at C/4.

J. Zheng, Q. Zhao, X. Liu, T. Tang, D.C. Bock, A.M. Bruck, K.R. Tallman, L.M. Housel, A.M. Kiss, A.C. Marschilok, E.S. Takeuchi, K.J. Takeuchi, L.A. Archer, *ACS Energy Lett.*, **2019,** *4(1),* 271-275.

Multifunctional Material Design: Reduction-Displacement

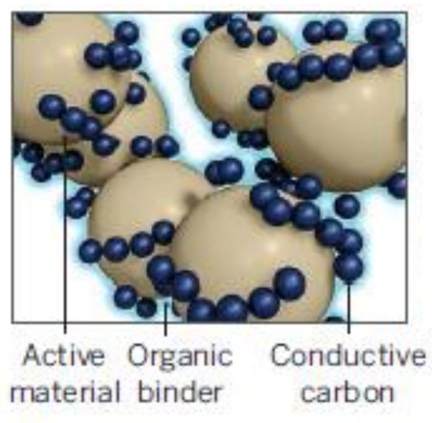

Composite electrode

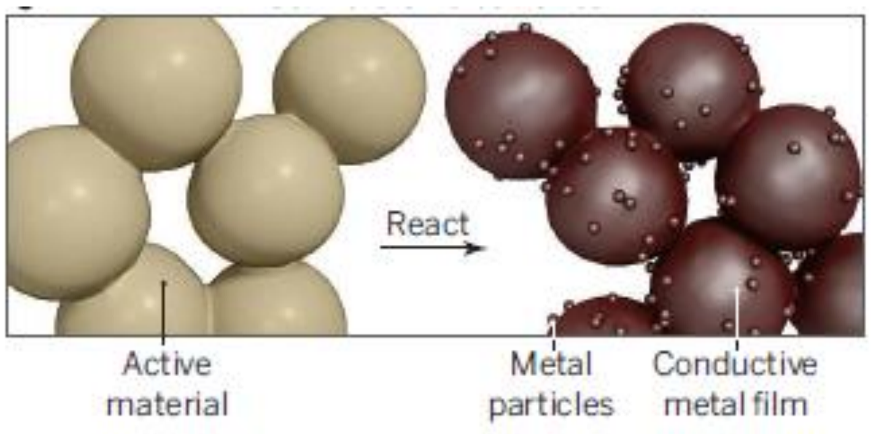

Formation of conductive matrix through reduction-displacement

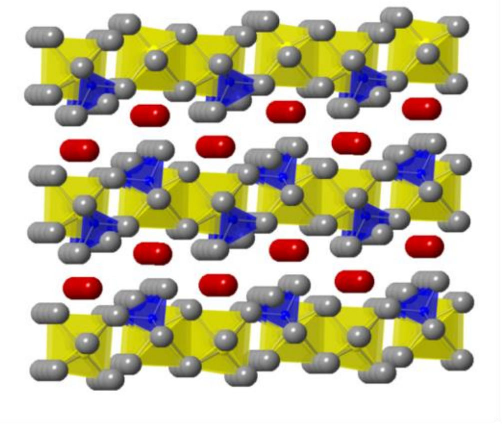

$Ag_xVO_y(PO_4)_z$

Ag V P O

Reduction of $Ag^+ \rightarrow Ag^0(s)$ during cathode discharge addresses conductivity of phosphate materials.

N. Dudney, J. Li, *Science,* **2015,** *347(6218),* 131.

Extending Life-Time of Battery by Eliminating Failure Mode

AC Impedance
Untreated (dashed)
V-treated (solid)

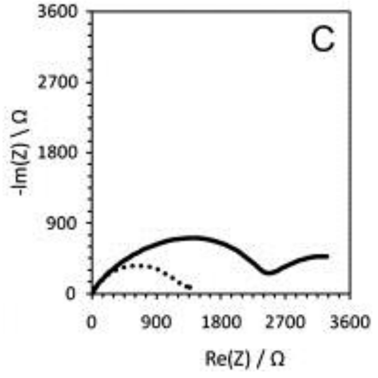

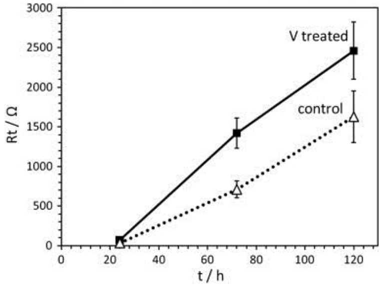

D.C. Bock, A.C. Marschilok, K.J. Takeuchi, E.S. Takeuchi, *J. Power Sources*, **2013,** *231,* 219-225.

X-ray absoption spectroscopy mapping and XANES enabled elucidation of anode surface composition and geography providing mechanistic insight regarding gradual ppm level cathode material disolution (over 1Y) manifesting as catastrophic cell polarization (over 10 s)

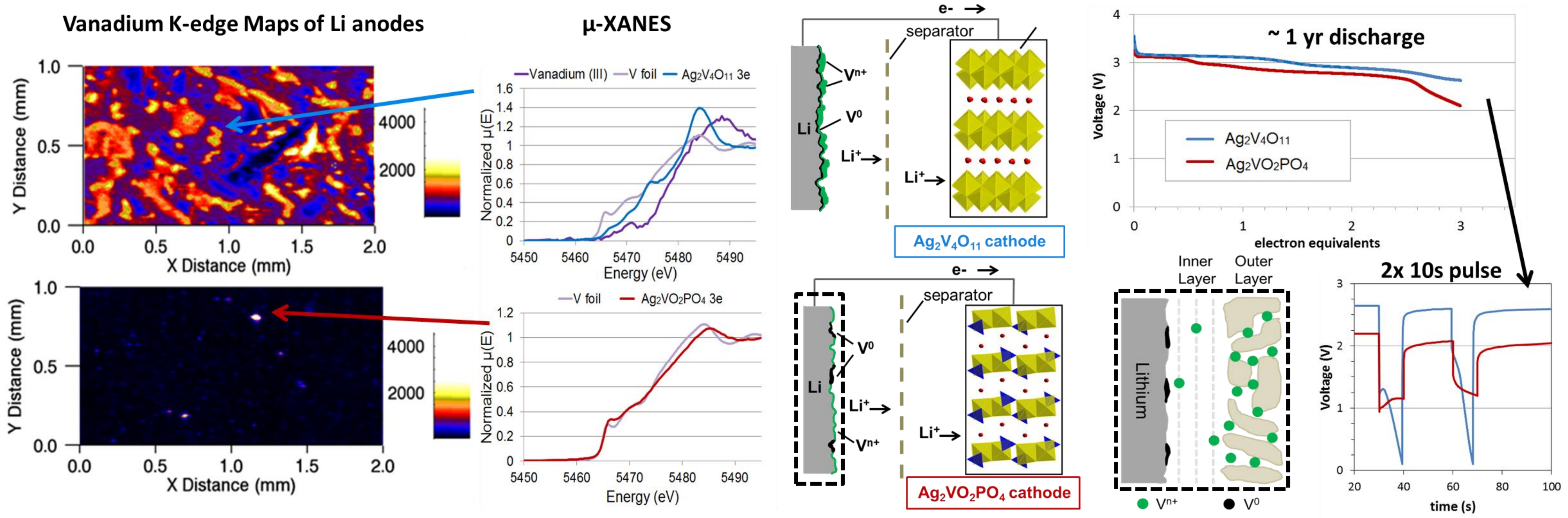

D.C. Bock, R.V. Tappero, K.J. Takeuchi, A.C. Marschilok, E.S. Takeuchi, *ACS Appl. Mater. Interfac.*, **2015,** *7(9),* 5429-5437.

Formation of Ag^0 via Reduction-Displacement

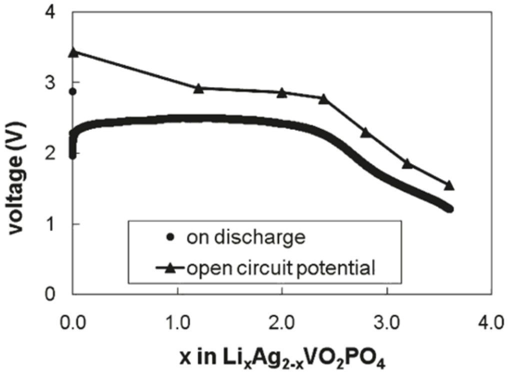

~4 e- transfer (272 mAh/g)

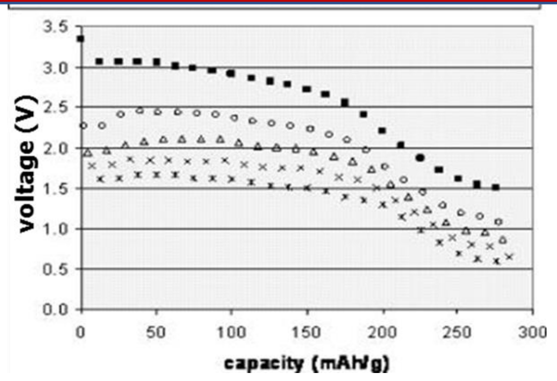

pulse up to 50 mA/cm^2

Resistance decreases by **15,000X** on initiation of reduction

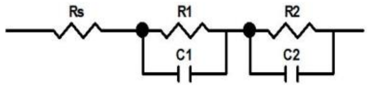

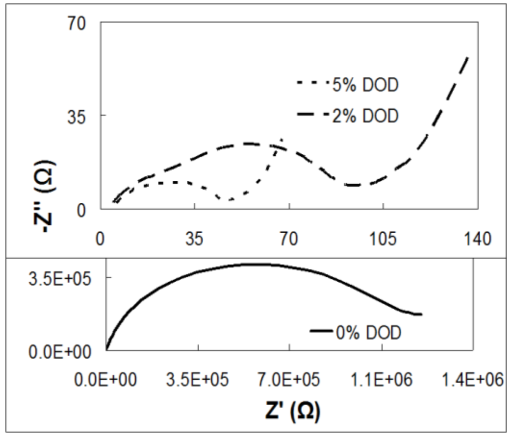

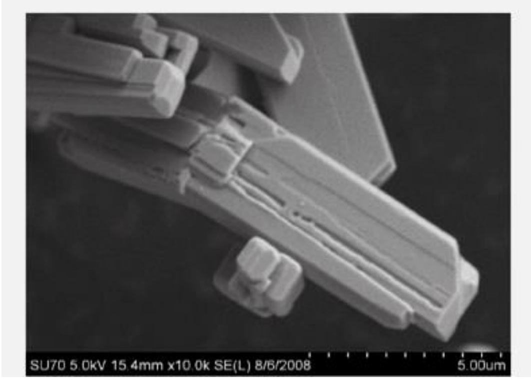

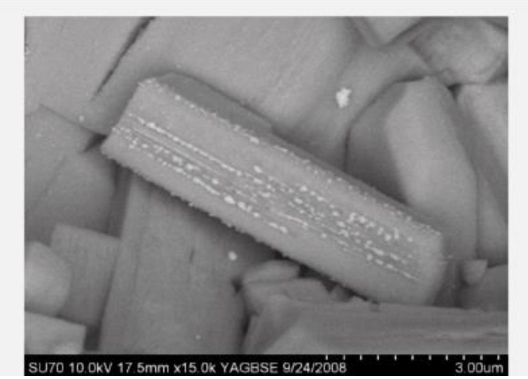

circuit element	0% discharge (Ω)	2% discharge (Ω)	5% discharge (Ω)
R_s	6.3	5.1	6.3
R1	18	22	19
R2	810,000	55	21

$$Ag_2VO_2PO_4 \xrightarrow{yLi\ (y<2)} Li_yAg_{2-y}VO_2PO_4 + yAg \xrightarrow{zLi\ (z>2)} Li_zVO_2PO_4 + 2Ag^0$$

A.C. Marschilok, K.J. Takeuchi, E.S. Takeuchi, *Electrochem. S.S. Lett.* **2009,** *12(1),* A5-A9.

E.S. Takeuchi, A.C. Marschilok, K. Tanzil, E.S. Kozarsky, S. Zhu, K.J. Takeuchi, *Chem. Mater.*, **2009**, *21*(20), 4934-4939.

Y.J. Kim, A.C. Marschilok, K.J. Takeuchi, E.S. Takeuchi, *J. Power Sources,* **2011,** *196(16)*, 6781-7.

Operando Visualization of Single Particle Electrochemistry

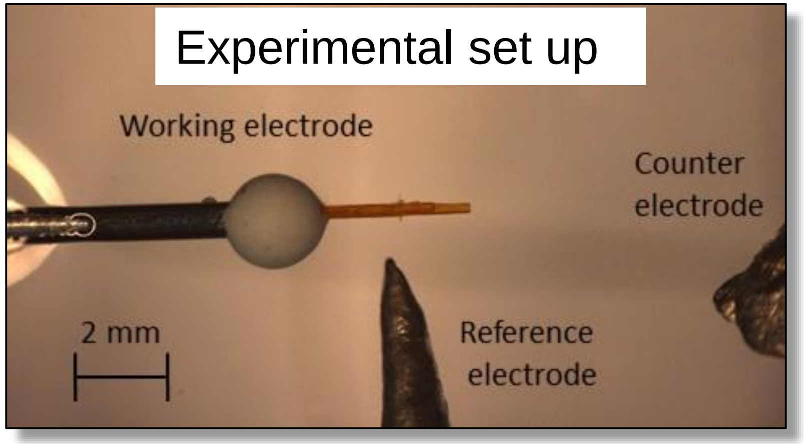

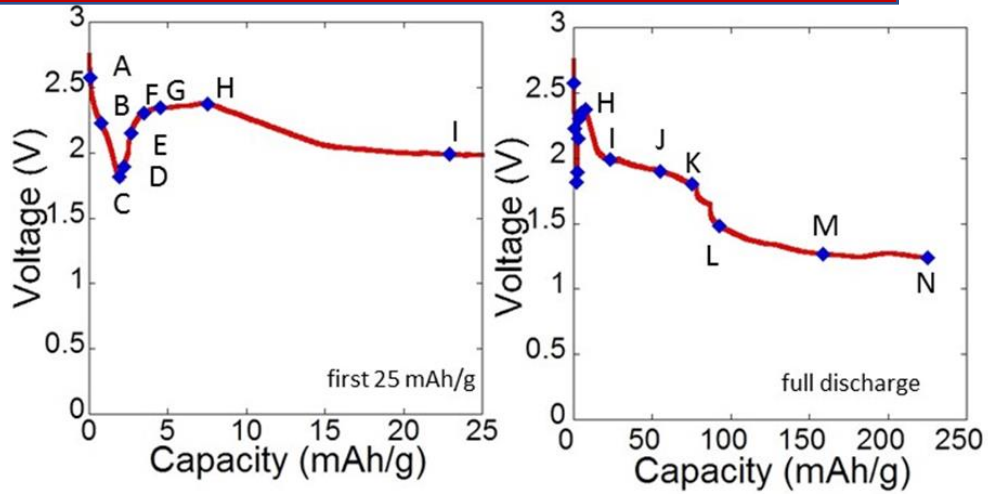

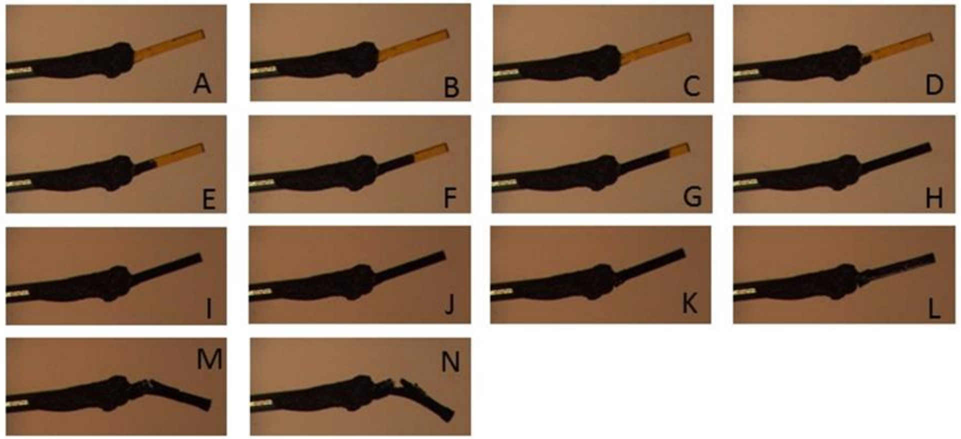

On discharge, voltage drops initially

- Polarization due to lack of electron access

At point C, Ag^0 begins to form

- Allows for electrons to access more of particle
- Voltage rises with access to undischarged material

K. Kirshenbaum, D. Bock, A. Brady, A. Marschilok, K. Takeuchi, and E. Takeuchi, *Phys. Chem. Chem. Phys.*, **2015,** *17(17),* 11204-11210.

Conductivity of Single Particle using Nanoprobe

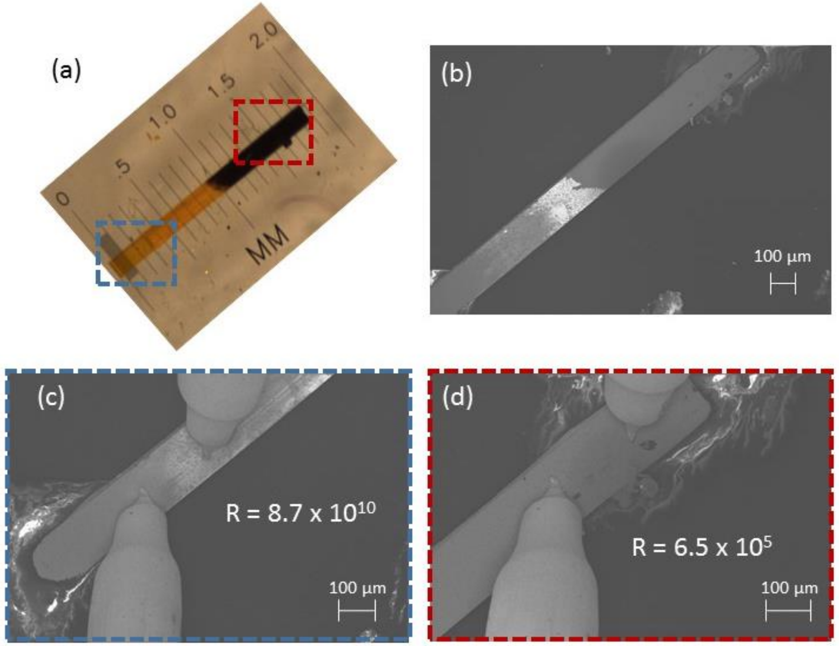

Particle details	Color of measured region	Resistance (Ω)	Distance between probes (µm)
Partially discharged particle	Black	6.5×10^5	196
	Orange	8.7×10^{10}	204
Partially discharged particle	Black	2.0×10^6	72
	Orange	2.9×10^{11}	68
Non-discharged particle	Orange	1.4×10^{12}	161
Non-discharged particle	Orange	5.2×10^{11}	173
Fully discharged (to approx. 250 mAh/g)	Black	8.2×10^6	187
	Black	7.5×10^6	318
	Black	7.8×10^6	546

Using STM tips, contacted surface, measured I-V curves

Black section shows 10^5-10^6 greater conductivity than orange section

Reduction including Ag metal formation greatly enhances conductivity and electron access

K. Kirshenbaum, D. Bock, A. Brady, A. Marschilok, K. Takeuchi, and E. Takeuchi, *Phys. Chem. Chem. Phys.*, **2015,** *17(17),* 11204-11210.

Discharge Rate affects Homogeneity

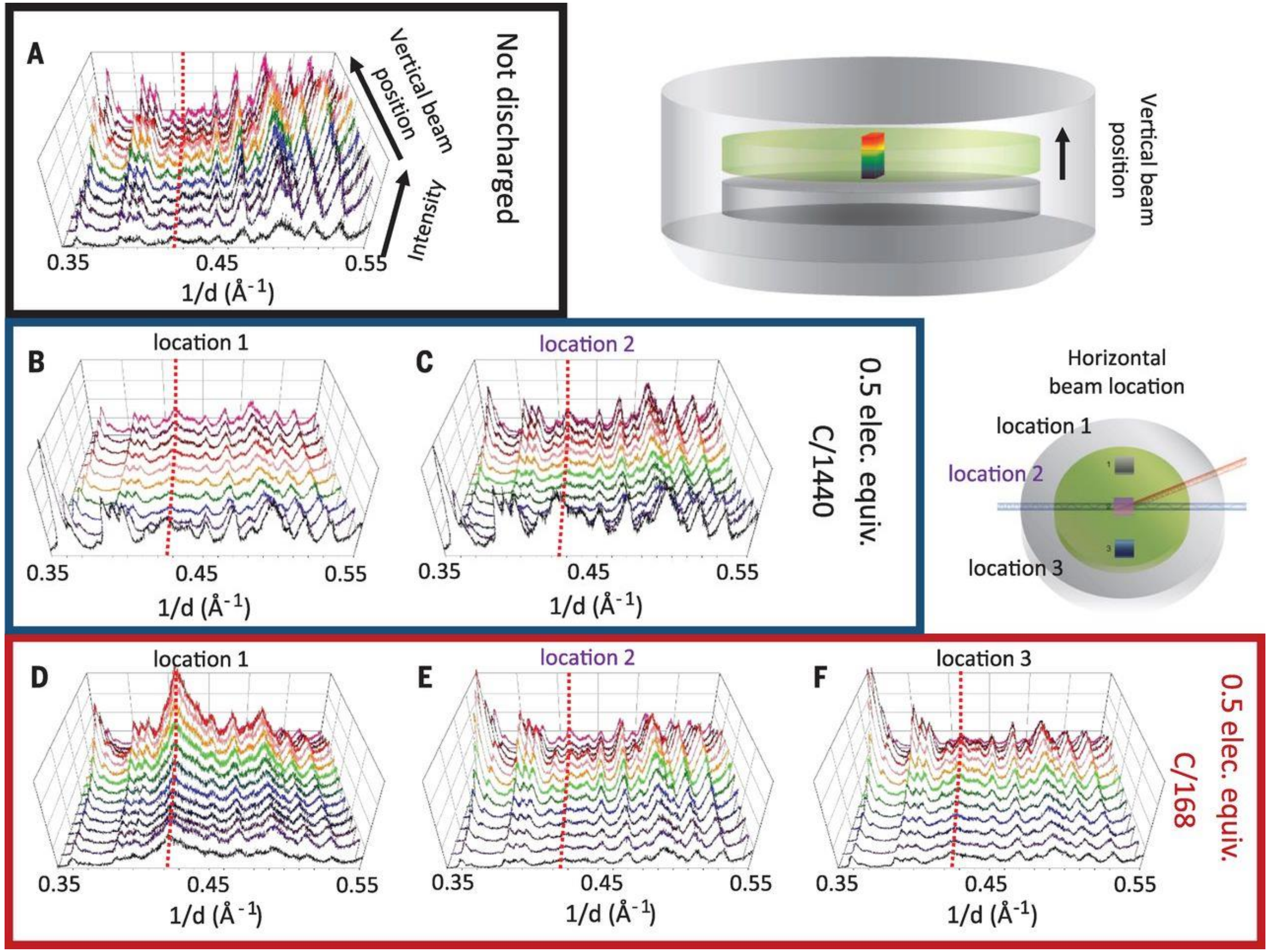

not discharged: uniform throughout, except 1st scan

C/1440 (slower) discharge: similar in both locations

C/168 (faster) discharge: Ag(111) intensity varies greatly among locations

K. Kirshenbaum, D.C. Bock, C.-Y. Lee, Z. Zhong, K.J. Takeuchi, A.C. Marschilok, E.S. Takeuchi, *Science,* **2015,** *347(6218),* 149.

Discharge Rate affects Homogeneity

C/168 (faster) discharge: Ag(111) intensity varies greatly among locations

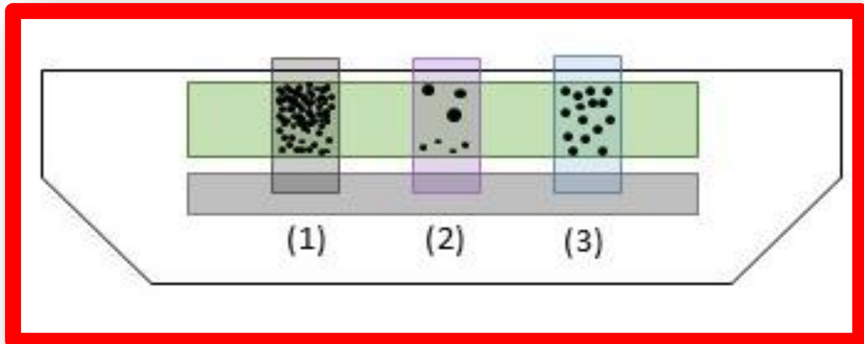

C/1440 (slower) discharge: similar in both locations

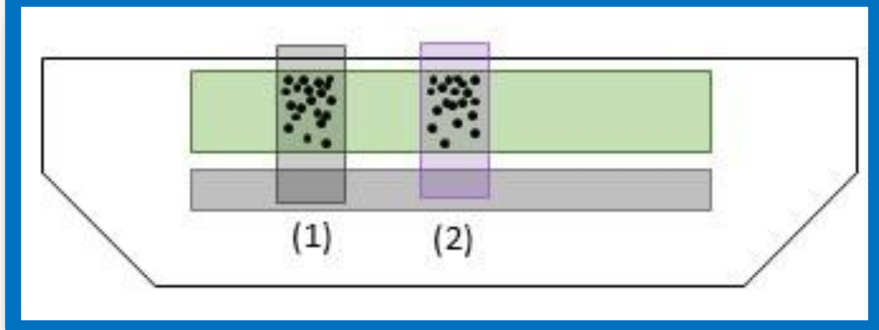

Fast discharge can result in non-uniform spatial distribution of Ag^0 with electronic isolation and incomplete utilization

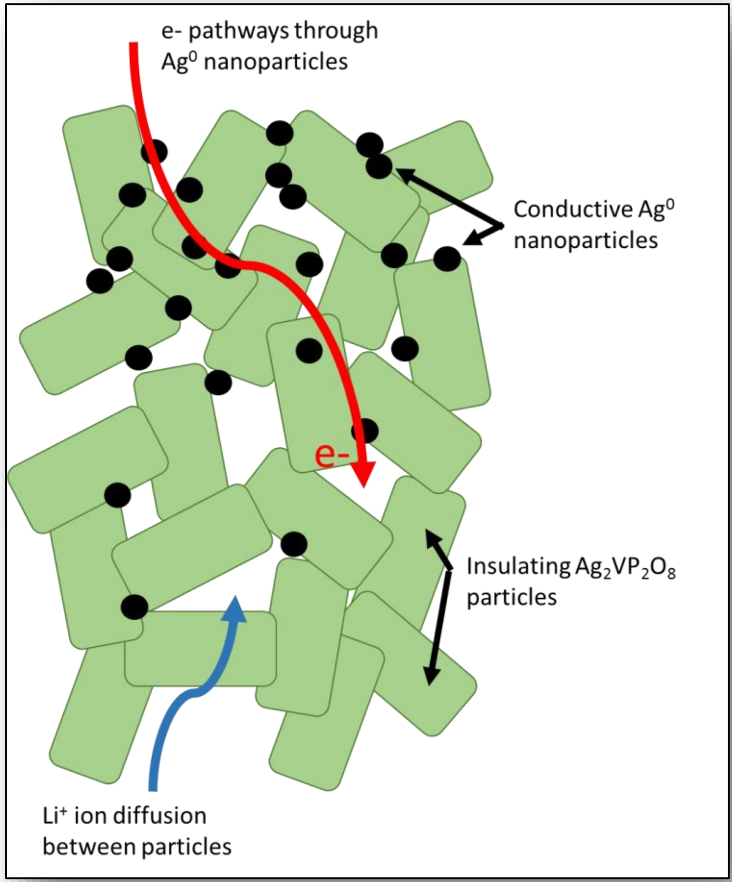

E. S. Takeuchi, A. C. Marschilok, K. J. Takeuchi, A. Ignatov, Z. Zhong, M. Croft, *Energy and Environ. Science*, **2013**, *6,* 1465.
Kirshenbaum, K. C.; Bock, D. C.; Zhong, Z.; Marschilok, A. C.; Takeuchi, K. J.; Takeuchi, E. S., *Phys. Chem. Chem. Phys.*, **2014,** *16(19),* 9138.

Trransport in Mesoscale composite SVPO + C + binder electrodes

Polymeric binder impedes transport resulting in negative impact on electrochemistry.

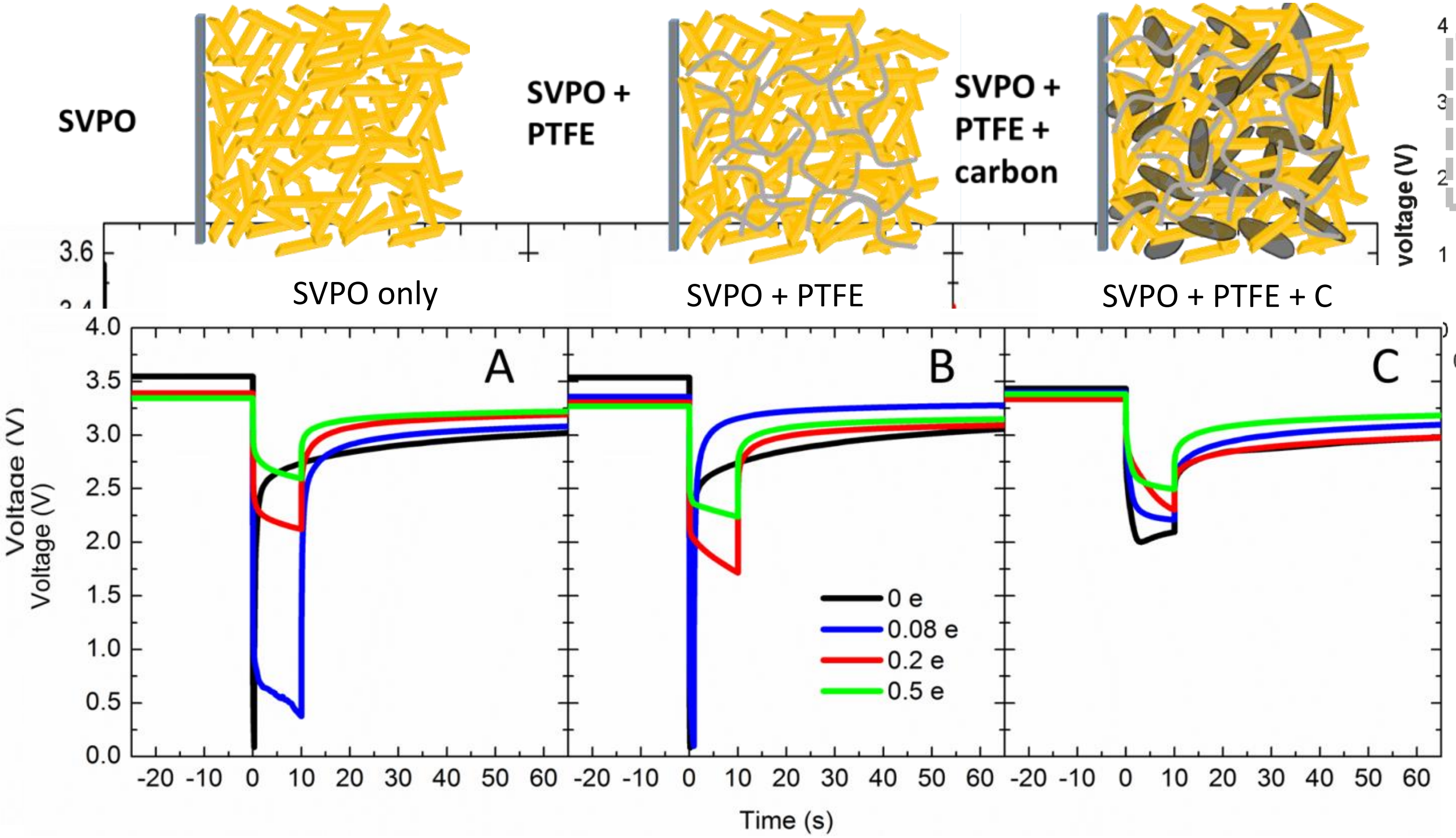

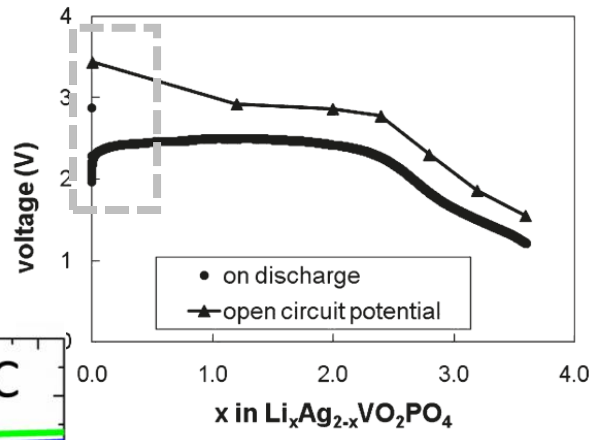

Cells w/o carbon deliver little to no energy < 0.2 electrons

Resistance of PTFE cells is greater at all stages of reduction

D. Bock, A. Bruck, C. Pelliccione, Y. Zhang, K.J. Takeuchi, A.C. Marschilok, E.S. Takeuchi, *RSC Adv.*, **2016,** *6,* 106887.

LiV_3O_8: A layered high capacity cathode material

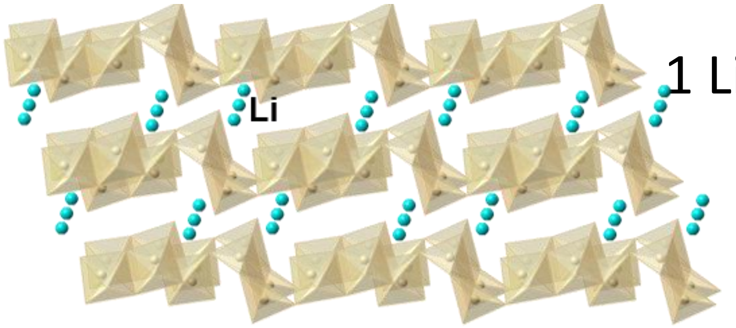

Layered cathode material comprised of V_3O_8 anionic layers in Oh sites, nLi^+ in Td sites in interlayer

Undergoes insertion upon electrochemical lithiation.

$$Li_{1.1}V_3O_8 + 3.9Li^+ + 3.9e^- \rightleftarrows Li_5V_3O_8$$

Appealing due to high theoretical capacity: 362 $mAh{\cdot}g^{-1}$ (3.9 electron eq.)

Previous XRD showed transition from parent phase (α) to defective rock-salt phase (β) upon lithiation

Previous DFT predicted α $Li_{1.5}V_3O_8$ and β $Li_4V_3O_8$ to be stable, with two phase region at ~$Li_{2.5}$ to Li_3

L. de Picciotto, K. Adendorff, D. Liles, M. Thackeray, *Solid State Ionics,* **1993,** *62,* (3-4), 297-307.
R. Benedek, M. Thackeray, L. Yang, *J. Power Sources,* **1999,** *81–82,* 487-490.
T. Jiang, M. Falk, *Physical Review B,* **2012,** 85, 245111.
S. Jouanneau, A. Verbaere, D. Guyomard, *J. Solid State Chem.,* **2005,** *178,* 22-27.
S. Sarkar, A. Bhowmik, M. D. Bharadwaj, S. Mitra, *J. Electrochem Soc.,* **2014,** *161,* A14-A22.
Z. Wang, J. Shu, Q. Zhu, B. Cao, H. Chen, X. Wu, B. Bartlett, K. Wang, J. Chen, *J. Power Sources,* **2016,** *307,* 426-434.

LiV_3O_8: Structural Change upon Lithiation

$$Li_{1.1}V_3O_8\,(\alpha) + 1.4\,e^- \rightleftharpoons Li_{2.5}V_3O_8\,(\alpha) \quad \textbf{(1)}$$

$$Li_{2.5}V_3O_8\,(\alpha) + 1.0\,e^-(or\ 1.5\,e^-) \rightleftharpoons Li_{3.5}V_3O_8\,(or\ Li_{4.0}V_3O_8)(\beta) \quad \textbf{(2)}$$

$$Li_{3.5}V_3O_8\,(or\ Li_{4.0}V_3O_8)(\beta) + 1.5\,e^-(or\ 1.0\,e^-) \rightleftharpoons Li_5V_3O_8\,(\beta) \quad \textbf{(3)}$$

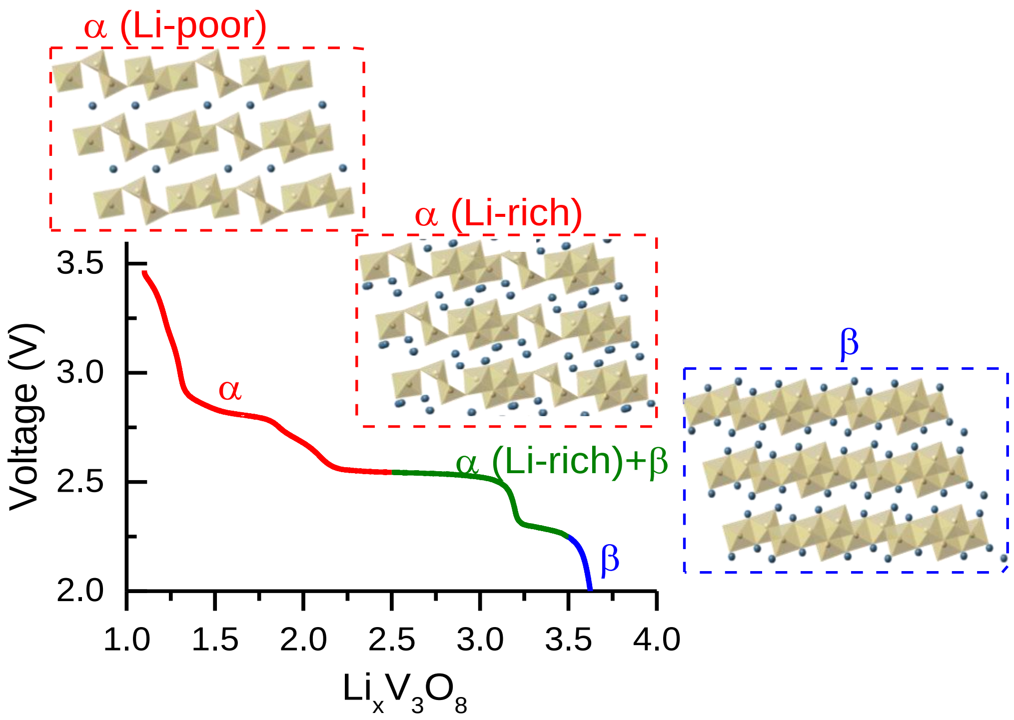

Li-poor α (LiV_3O_8): Stacked V_3O_8 layers with Li^+ residing in the interlayer space.

Li-rich α ($Li_{2.5}V_3O_8$): Same stacked V_3O_8 layers as Li-poor α, however more distorted with elongated *b* axis and shortened *a* axis.

β ($Li_4V_3O_8$): Defective rock-salt structure. V and Li have octahedral coordination.

On Li-rich α-phase to β-phase transformation, Li^+ ions in Td environments shift to Oh sites, and O^{2-} ions displace to adopt a more cubic close packed structure

Q. Zhang, A.B. Brady, C.J. Pellicione, D.C. Bock, A.M. Bruck, J. Li, V. Sarbada, R. Hull, E.A. Stach, K.J. Takeuchi, E.S. Takeuchi, P. Liu, A.C. Marschilok, *Chem. Mater.*, **2017**, *29(5),* 2364-2373.

Li/LiV$_3$O$_8$: Operando ADXRD

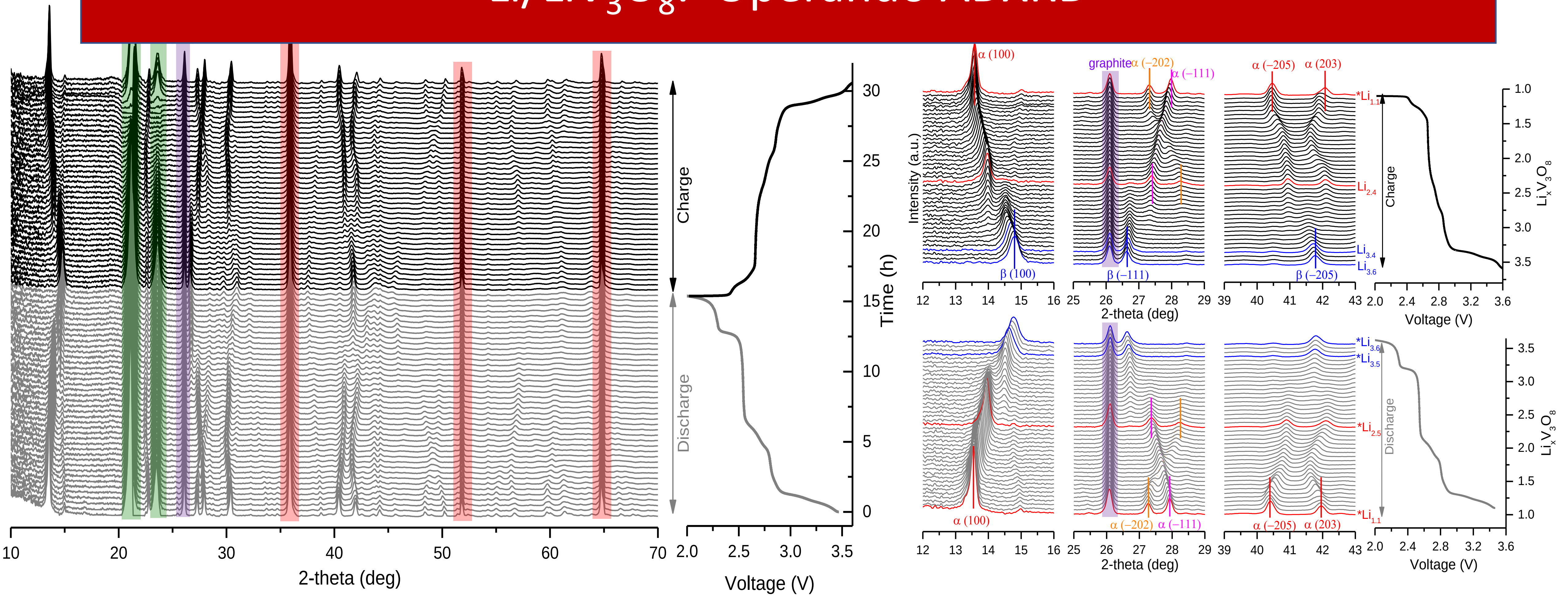

Discharge - single phase lithiation of α to $Li_{2.5}V_3O_8$, α-β to $Li_{3.5}V_3O_8$, then single phase β.

Charge - phase transformations structurally similar to those during discharge.

Li/LiV_3O_8: Crystal scale transport dominates

Significant mass transfer resistances occur on the crystal scale, consistent with assumption of 1-D diffusion along the [001] direction upon discharge

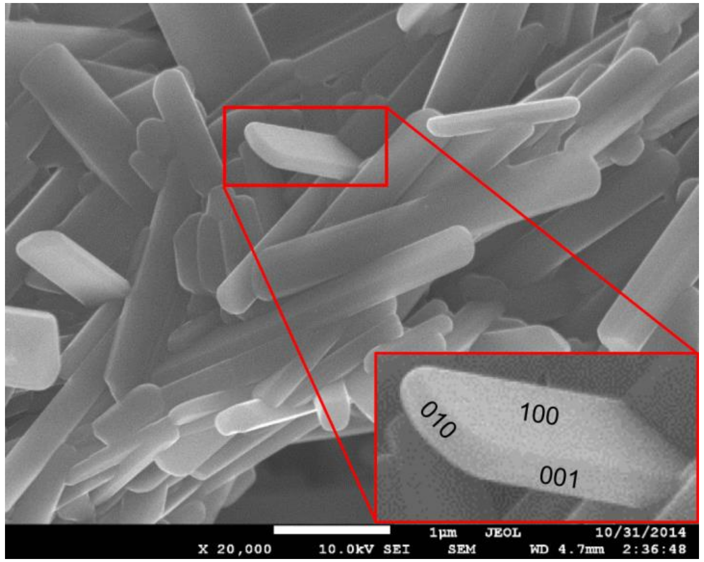

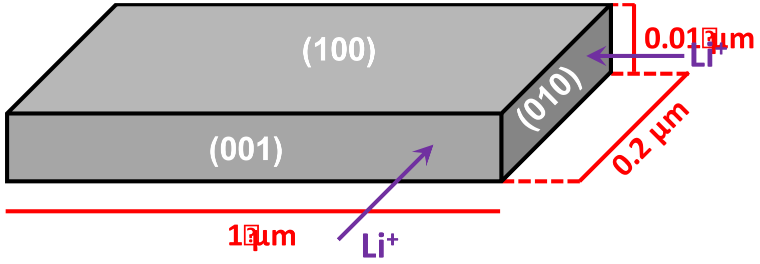

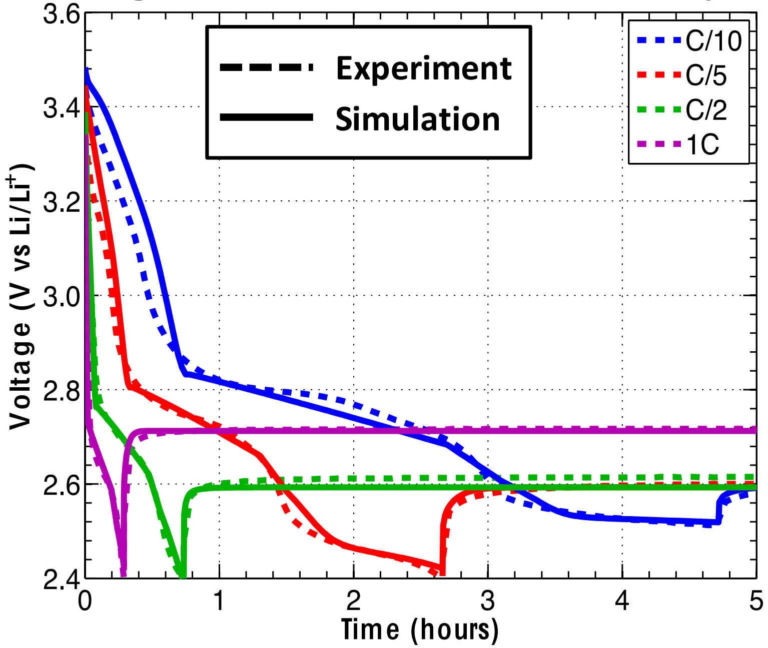

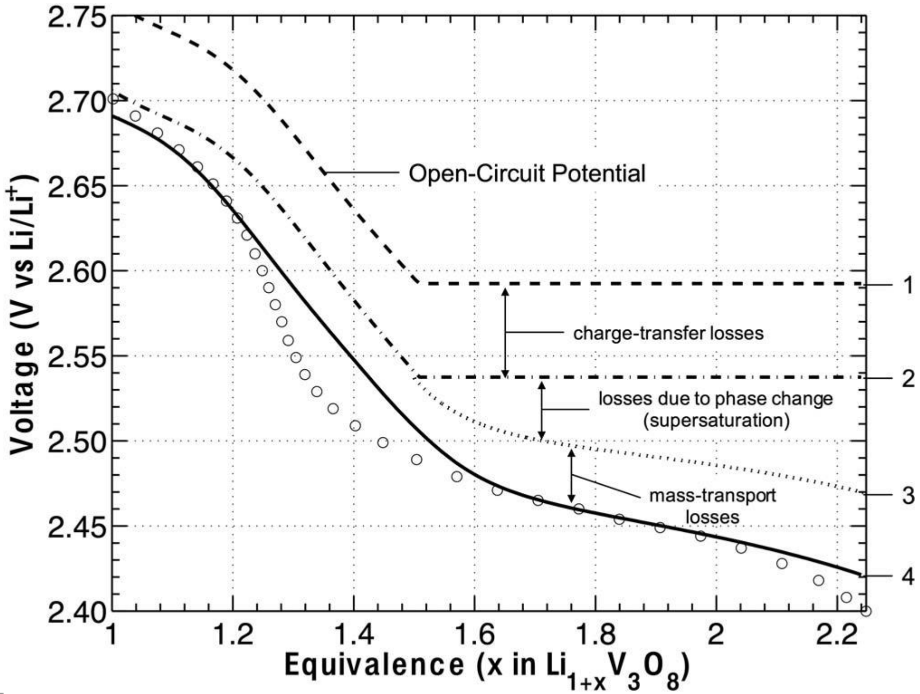

Phase Change Kinetics

$$\frac{\partial \theta_\beta}{\partial t} = k_\beta (c_\alpha - c_{\alpha,sat}) \theta_\beta^m [1 - \theta_\beta]$$

Charge Transfer

$$i = i_0 \left[\exp\left(\frac{\alpha_a F \eta}{R_G T}\right) - \exp\left(-\frac{\alpha_c F \eta}{R_G T}\right) \right]$$

Phase change based on Avrami's model of nucleation and growth

Charge transfer based on Butler-Volmer

N. Brady, Q. Zhang, K. Knehr, P. Liu, A.C. Marschilok, K.J. Takeuchi, E.S. Takeuchi, A.C. West. *J. Electrochem. Soc.*, **2016**, *163(14),* A2890-A2898.

Thick LiV_3O_8 electrodes require electrode scale considerations

Crystallite scale effects remain important
Must also account for electrode scale effects

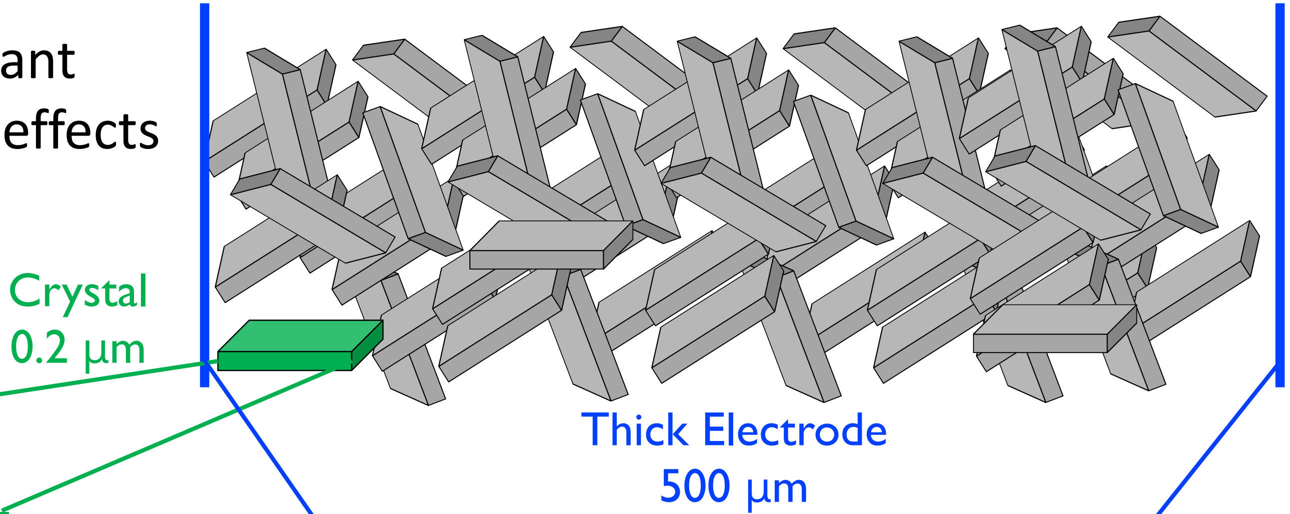

Crystallite Scale Considerations
Lithium Concentration in the α-Phase
Balance on β-Phase Formation
Electrochemical Reaction Rate

Electrode Scale Considerations
Electrolyte Current (i_2)
Solid-State Current (i_1)
Electrolyte Concentration

N.W. Brady, Q. Zhang, A.M. Bruck, D.C. Bock, C.A. Gould, A.C. Marschilok, K.J. Takeuchi, E.S. Takeuchi, A.C. West.
J. Electrochem. Soc., **2018**, *165(2),* A371.

Importance of Operando Measurements

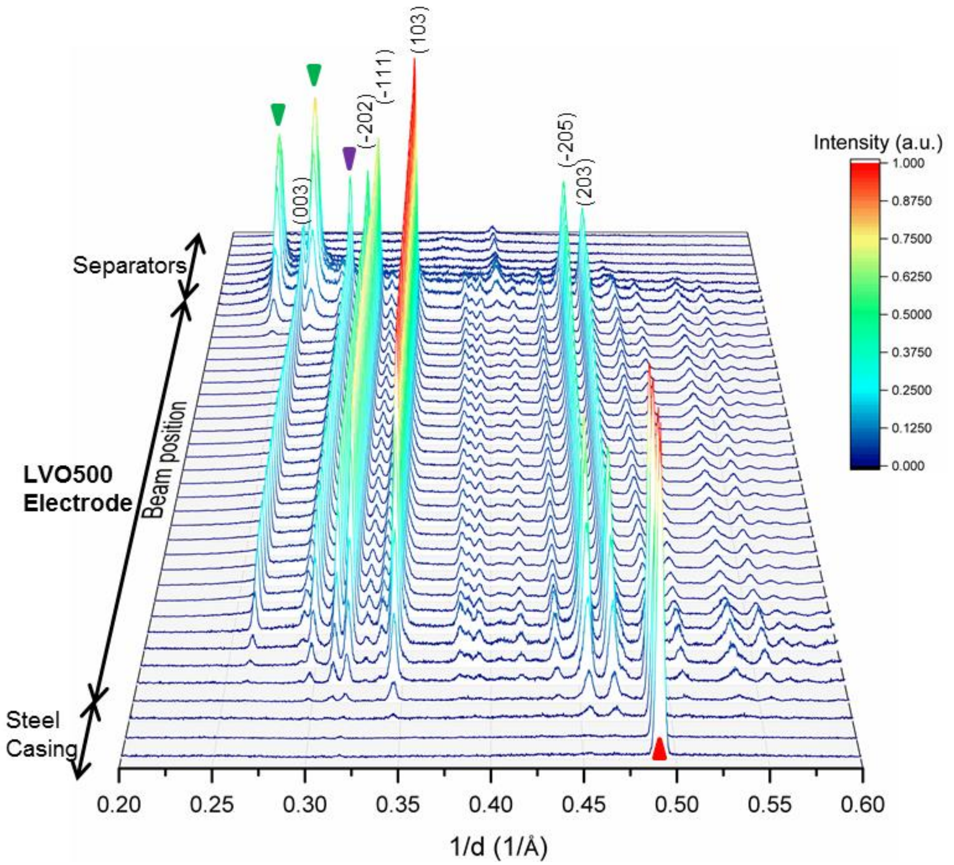

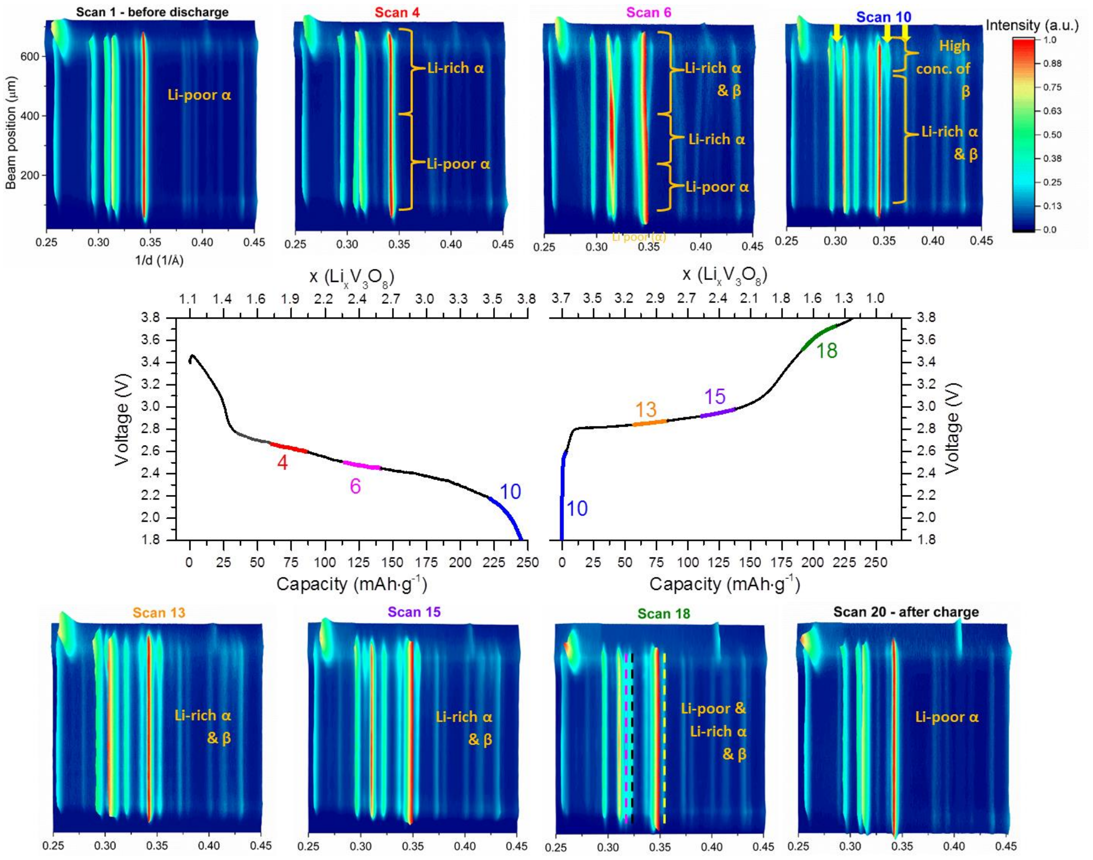

First visualization of phase evolution in LVO during *operando* lithiation via EDXRD.

Lithiation initiated near the Li anode then proceeded towards the cathode current collector interface.

Q. Zhang, A.M. Bruck, D.C. Bock, J. Li, V. Sarbada, R. Hull, E.A. Stach, K.J. Takeuchi, E.S. Takeuchi, A.C. Marschilok. *Phys. Chem. Chem. Phys.,* **2017,** *19,* 14160-14169.

3D V_2O_5 Electrode Regeneration

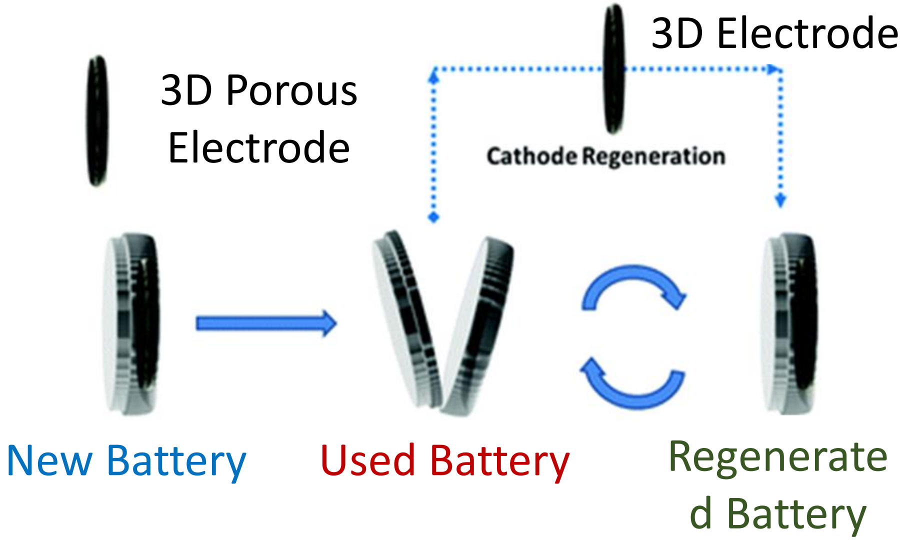

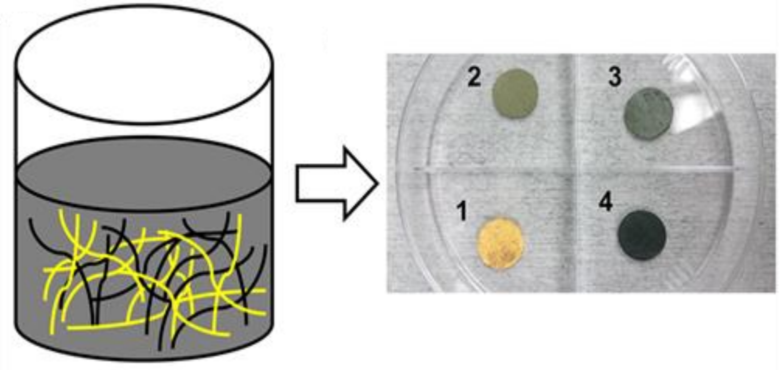

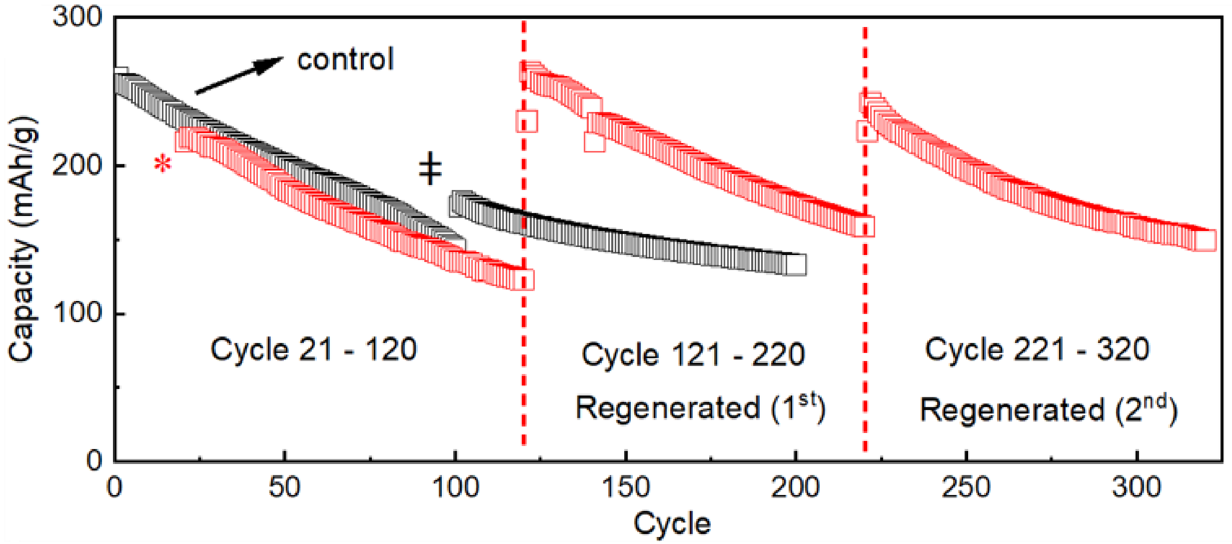

Capacity increase after heating extends cycle life for V_2O_5 3D porous electrodes

J.P. Huang†, L.M. Housel†, L. Wang, A.M. Bruck, C.D. Quilty, A. Abraham, D.M. Lutz, C.R. Tang, A. Kiss, J. Thieme, K.J. Takeuchi, E.S. Takeuchi, A.C. Marschilok, *Sustainable Energy & Fuels*, **2019**, *3(10)*, 2615-2626.

Structural Evolution Before and After Regeneration

Before Regeneration

After Regeneration

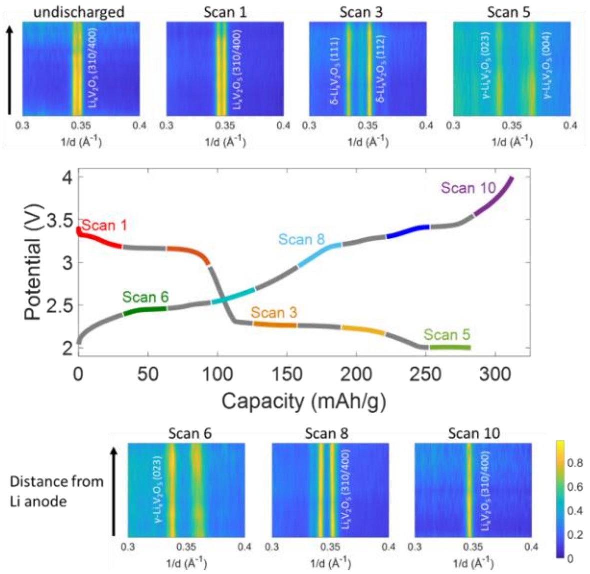

Irreversible α- ε- δ- γ- ω transition

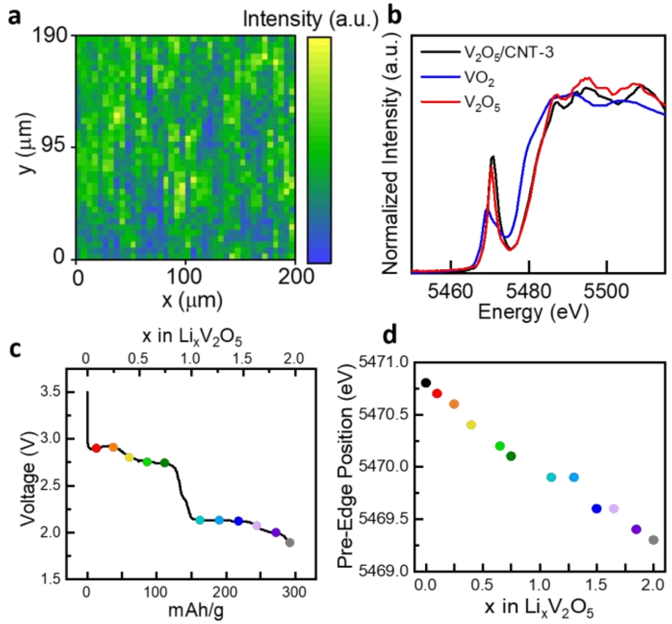

V^{5+} to V^{4+} reduction

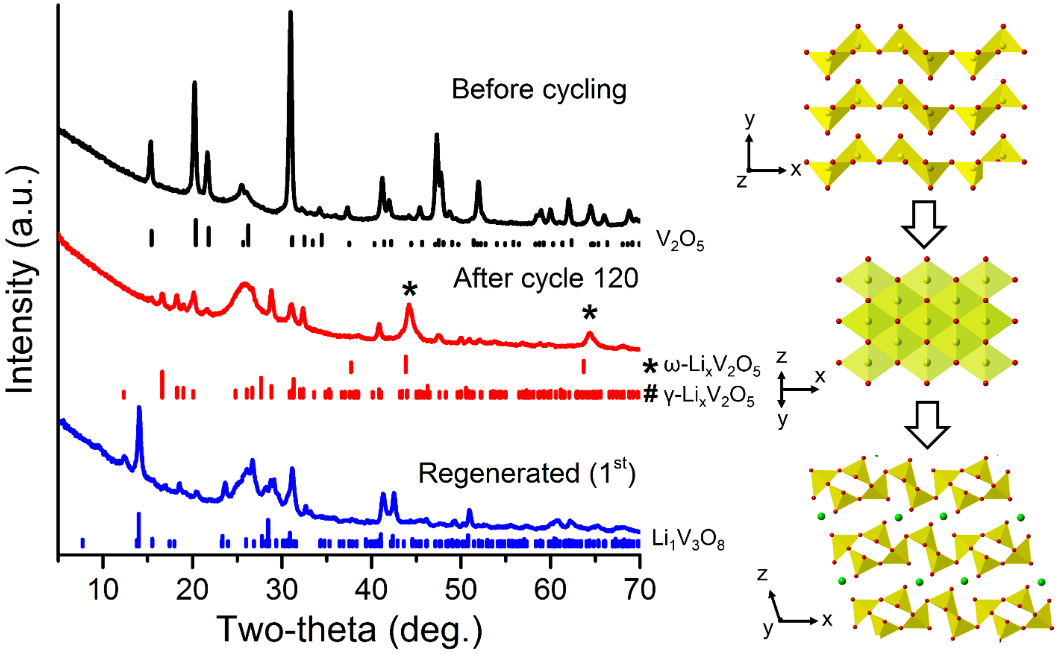

Reversible $Li_1V_3O_8$ to γ-$Li_xV_2O_5$ transition

J.P. Huang┼, L.M. Housel┼, L. Wang, A.M. Bruck, C.D. Quilty, A. Abraham, D.M. Lutz, C.R. Tang, A. Kiss, J. Thieme, K.J. Takeuchi, E.S. Takeuchi, A.C. Marschilok, *Sustainable Energy & Fuels,* **2019,** *3(10),* 2615-2626.

Summary

Structure, crystallite size, and agglomerate size matter, impacting ion transport during both initial lithiation and reversibility of conversion.

Onset of SEI formation can be elucidated through complementary information from *operando* microcalorimetry and *operando* XAS methods.

Tomographic information about phase evolution provides valuable insight on transport for thick and 3-Dimensional electrodes, critical for determination of factors governing electrochemistry in high energy density scalable batteries.

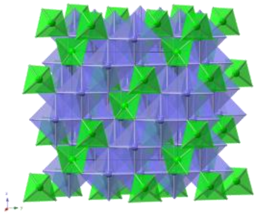

Fe_3O_4

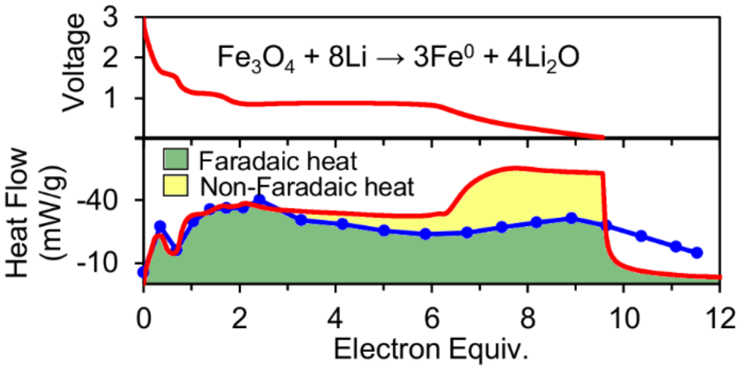

LFP

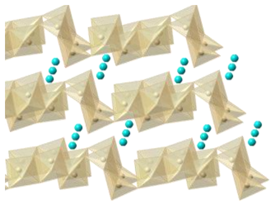

LVO

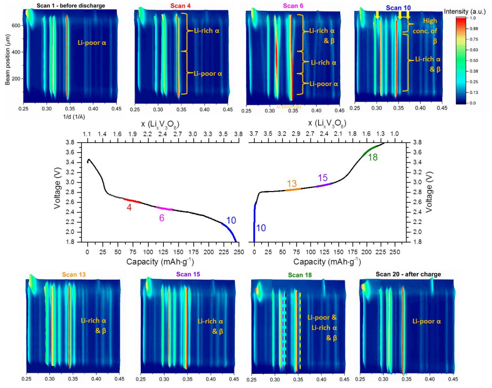

Acknowledgements

Marschilok/Takeuchi Research Group

EFRC Team: Center for Mesoscale Transport Properties

Acknowledgements

Center for Mesoscale Transport Properties, an Energy Frontier Research Center supported by the U.S. Department of Energy, Office of Science, Basic Energy Sciences, award #DE-SC0012673.

m2m molecular to mesoscale

m2m/t molecular to mesoscale over time

National Heart Lung and Blood Institute

National Institutes of Health

NEW YORK STATE OF OPPORTUNITY. | NYSERDA

NEW YORK STATE OF OPPORTUNITY. | ESD

U.S. DEPARTMENT OF ENERGY Office of ENERGY EFFICIENCY & RENEWABLE ENERGY

Mercedes-Benz

Research and Development North America

William and Jane Knapp Chair in Energy and the Environment

Sandia National Laboratories

Office of Electricity Delivery & Energy Reliability

NSF GRFP

Contrast In-situ versus Operando Insights

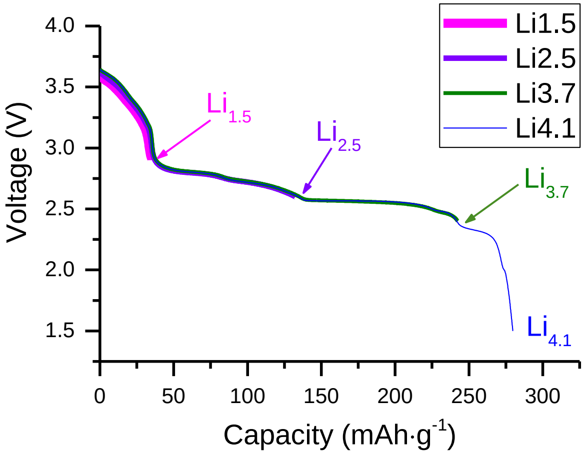

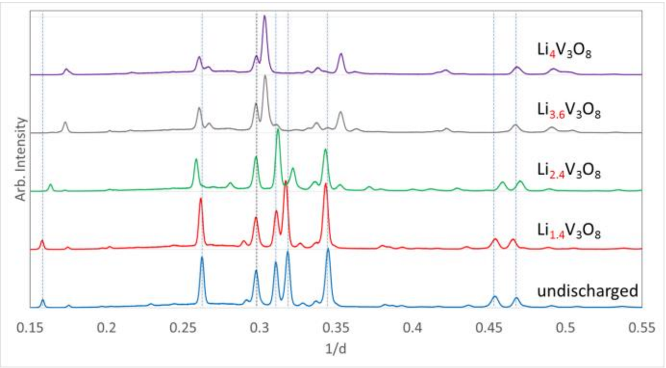

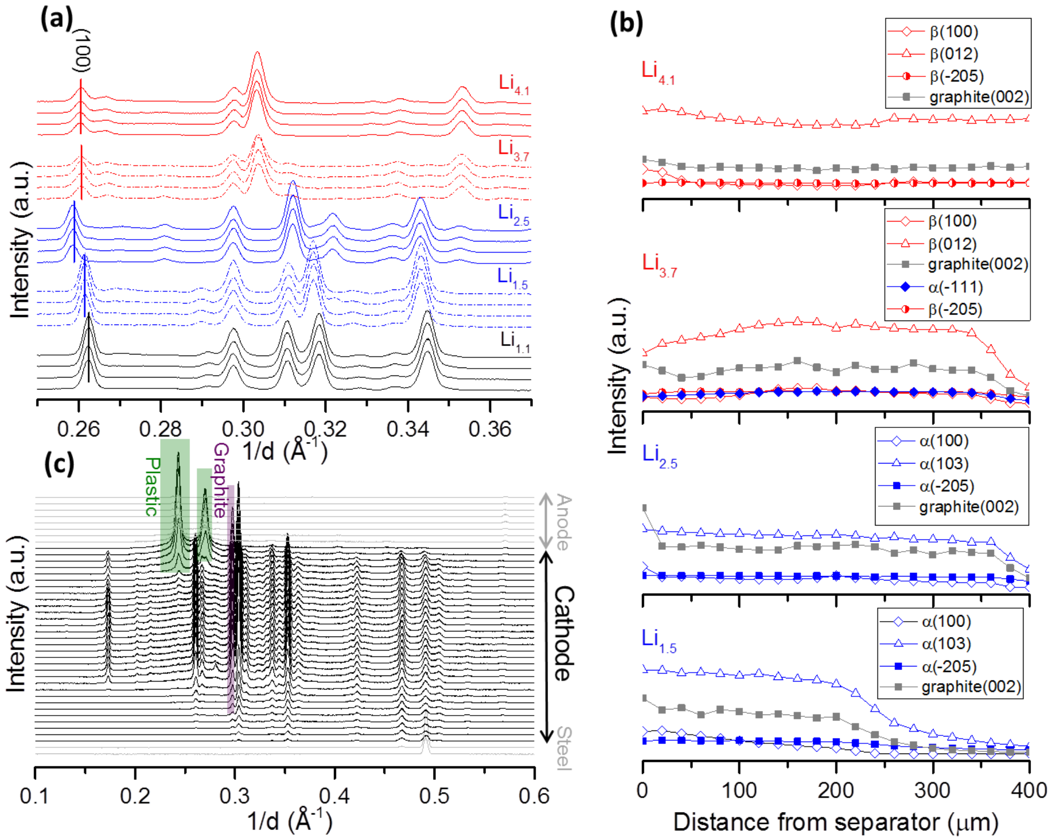

Homogeneity through the electrode thickness (z) at each depth of discharge, consistent with full utilization.

Can distinguish α and β phases, however no spatial localization of phase formation observed through the electrode thickness.

(a) Four scans of each cell ($Li_{1.1}V_3O_8$, $Li_{1.5}V_3O_8$, $Li_{2.5}V_3O_8$, $Li_{3.7}V_3O_8$ and $Li_{4.1}V_3O_8$) at 40, 140, 240, and 340 microns from the separator; (b) Intensity change of selected peaks with respect to location of the electrodes. (c) Full scan of the cell discharged to $Li_{3.7}$.

Q. Zhang, A.M. Bruck, D.C. Bock, J. Li, E.A. Stach, E.S. Takeuchi, K.J. Takeuchi, A.C. Marschilok, *MRS Adv.,* **2017,** *2(7),* 401-406.